Article

# Coupling of Indo-Pacific climate variability over the last millennium

https://doi.org/10.1038/s41586-020-2084-4

Received: 3 May 2019

Accepted: 18 December 2019

Published online: 9 March 2020

Check for updates

Nerilie J. Abram[1,2]✉, Nicky M. Wright[1,2], Bethany Ellis[1,3], Bronwyn C. Dixon[1,3,4], Jennifer B. Wurtzel[1,15], Matthew H. England[5,6], Caroline C. Ummenhofer[6,7], Belle Philibosian[8], Sri Yudawati Cahyarini[9], Tsai-Luen Yu[10,11], Chuan-Chou Shen[10,11,12], Hai Cheng[13,14], R. Lawrence Edwards[14] & David Heslop[1]

The Indian Ocean Dipole (IOD) affects climate and rainfall across the world, and most severely in nations surrounding the Indian Ocean[1–4]. The frequency and intensity of positive IOD events increased during the twentieth century[5] and may continue to intensify in a warming world[6]. However, confidence in predictions of future IOD change is limited by known biases in IOD models[7] and the lack of information on natural IOD variability before anthropogenic climate change. Here we use precisely dated and highly resolved coral records from the eastern equatorial Indian Ocean, where the signature of IOD variability is strong and unambiguous, to produce a semi-continuous reconstruction of IOD variability that covers five centuries of the last millennium. Our reconstruction demonstrates that extreme positive IOD events were rare before 1960. However, the most extreme event on record (1997) is not unprecedented, because at least one event that was approximately 27 to 42 per cent larger occurred naturally during the seventeenth century. We further show that a persistent, tight coupling existed between the variability of the IOD and the El Niño/Southern Oscillation during the last millennium. Indo-Pacific coupling was characterized by weak interannual variability before approximately 1590, which probably altered teleconnection patterns, and by anomalously strong variability during the seventeenth century, which was associated with societal upheaval in tropical Asia. A tendency towards clustering of positive IOD events is evident in our reconstruction, which—together with the identification of extreme IOD variability and persistent tropical Indo-Pacific climate coupling—may have implications for improving seasonal and decadal predictions and managing the climate risks of future IOD variability.

The IOD is a mode of interannual climate variability in the tropical Indian Ocean that originates from ocean–atmosphere interactions that are similar to those of El Niño/Southern Oscillation (ENSO) variability in the tropical Pacific[3,8]. The IOD was first formally defined in 1999, following the extreme positive IOD events of 1994 and 1997 (refs. [1,2]). Positive IOD events are initiated by the development of enhanced ocean upwelling along the Javan and Sumatran coasts in the eastern Indian Ocean. This generates anomalously cool sea surface temperatures (SSTs) in the east, resulting in strengthened easterly winds along the Equator, enhanced ocean warming in the western Indian Ocean and an associated increase (decrease) in atmospheric Walker cell convection over the western (eastern) tropical Indian Ocean[2]. IOD activity is seasonally phase-locked by the wind reversals associated with Northern Hemisphere summer monsoon airflow towards India and Asia and, once established, ocean–atmosphere feedbacks sustain and strengthen positive IOD anomalies until the reversal of the trade winds in November[3]. The IOD causes worldwide impacts, which are particularly severe in the regions surrounding the Indian Ocean basin[1–4]. IOD variability is implicated in Australia's worst droughts[9], as well as wildfire risk and habitat destruction in Indonesia and southeast Australia[2,10,11]. Positive IOD events have also been linked to floods and malaria outbreaks in eastern Africa[2,12].

[1]Research School of Earth Sciences, The Australian National University, Canberra, Australian Capital Territory, Australia. [2]ARC Centre of Excellence for Climate Extremes, The Australian National University, Canberra, Australian Capital Territory, Australia. [3]ARC Centre of Excellence for Climate System Science, The Australian National University, Canberra, Australian Capital Territory, Australia. [4]School of Geography, University of Melbourne, Melbourne, Victoria, Australia. [5]Climate Change Research Centre, University of New South Wales, Sydney, New South Wales, Australia. [6]ARC Centre of Excellence for Climate Extremes, University of New South Wales, Sydney, New South Wales, Australia. [7]Department of Physical Oceanography, Woods Hole Oceanographic Institution, Woods Hole, MA, USA. [8]Earthquake Science Center, United States Geological Survey, Menlo Park, CA, USA. [9]Research Centre of Geotechnology, Indonesian Institute of Sciences (LIPI), Bandung, Indonesia. [10]High-precision Mass Spectrometry and Environment Change Laboratory (HISPEC), Department of Geosciences, National Taiwan University, Taipei, Taiwan. [11]Research Center for Future Earth, National Taiwan University, Taipei, Taiwan. [12]Global Change Research Center, National Taiwan University, Taipei, Taiwan. [13]Institute of Global Environmental Change, Xi'an Jiaotong University, Xi'an, China. [14]Department of Geology and Geophysics, University of Minnesota, Minneapolis, MN, USA. [15]Present address: New South Wales Department of Primary Industries, Orange, New South Wales, Australia. ✉e-mail: nerilie.abram@anu.edu.au

The frequency and effects of positive IOD events are expected to increase with climate warming[3,6,13]. An unusual increase in both the number and intensity of positive IOD events after about 1960 has been identified in reconstructions of IOD variability since the mid-nineteenth century[5]. Accelerated warming of the western Indian Ocean and shoaling of the thermocline in the east are expected to promote a future mean climate state in the Indian Ocean that is more conducive to the development of positive IOD events[3]. Additionally, nonlinear rainfall impacts are expected to worsen the climate risks associated with extreme positive IOD events[6]. Climate model assessments indicate that the aim of limiting global warming to 1.5 °C of the Paris Agreement would result in the stabilization of the extreme positive IOD event frequency at double that of pre-industrial times[14], whereas unabated warming during the twenty-first century could result in a tripling of the frequency of extreme positive IOD events[6].

Despite the apparent consistency between observed and projected changes in IOD variability, many challenges still exist in assessing IOD responses and associated risks in a warming world. Climate models are known to have biases that favour the development of positive IOD events too frequently and too strongly. These biases are thought to be caused by Bjerkness-like feedbacks that are too strong in current climate models and that may limit the accuracy of projected rainfall changes in IOD-affected regions[7]. Furthermore, the short observational and palaeoclimate reconstruction history of the IOD may not capture the full range of unforced (internal) IOD variability[1,5,8], making robust attribution of recent trends to anthropogenic climate forcing difficult. Assessments of ENSO variability indicate that multiple centuries of data are required to detect forced changes in this climate mode[15,16]. It remains unclear to what extent unforced natural variability might similarly affect the detection of forced changes in the IOD.

Here we use a collection of monthly resolved and precisely dated coral records from the equatorial eastern Indian Ocean to reconstruct IOD variability during the last millennium. This new dataset allows us to characterize the temporal evolution and range of natural variability of the IOD, to assess long-term relationships between the IOD and Pacific climate variability, and to identify future avenues for managing the climate risks caused by the IOD.

## Modern coral record of the IOD

The coral samples used in this study are derived from the southern Mentawai Island chain, offshore of Sumatra (Fig. 1; Methods; Extended Data Fig. 1). This area lies within the ocean-upwelling region of the eastern Indian Ocean that is fundamental to IOD variability[17], and is where positive IOD events are associated with prominent cool and dry anomalies (Fig. 1a, b; Extended Data Fig. 2). IOD variability is traditionally described through the Dipole Mode Index (DMI), calculated as the west–east difference in SST anomalies across the equatorial Indian Ocean[1] (Fig. 1c; Methods). Oxygen isotope ($\delta^{18}O$) records from modern *Porites* corals growing within or near to the eastern and western DMI regions have been used to reconstruct a coral-based DMI since 1846[5]. However, this approach cannot be used for fossil *Porites* coral sequences during the last millennium owing to the absence of coeval and precisely dated fossil coral specimens in both DMI regions[18]. Instead, it has been previously shown that corals from the southern Mentawai Island chain are optimal for reconstructing IOD variability at a single site, and that coral $\delta^{18}O$ variability at this location reliably preserves information about the occurrence and magnitude of positive IOD events[18].

A modern coral $\delta^{18}O$ record collected from our study site in July 2001 reveals the preservation of IOD-related climate signals (Fig. 1d; Extended Data Fig. 1). Coral $\delta^{18}O$ reflects both the temperature of the ocean water that the coral grew in and changes in the hydrological cycle that altered the isotopic composition of the surface ocean water[19,20]. Nonlinear rainfall impacts occur in the central equatorial Indian Ocean in response to IOD variability[6]. However, observational data and climate model output indicate that in the eastern upwelling region of optimal IOD variability the cool SST anomalies associated with positive IOD events scale linearly to rainfall depletion anomalies and are stable over time (Extended Data Fig. 3; Methods). Atmospheric coupling is therefore not expected to bias our assessments of positive IOD events recorded by coral $\delta^{18}O$. The modern coral $\delta^{18}O$ record is significantly correlated with satellite-derived SST ($r = -0.86$, $P < 0.01$, effective sample size $n_{eff} = 18$; 1982–2000) and rainfall ($r = -0.81$, $P < 0.01$, $n_{eff} = 21$; 1979–2000) at the study site during the July–December half-year when positive IOD events can occur (Extended Data Fig. 1). To examine the interannual variability of the IOD, the coral $\delta^{18}O$ and DMI data are filtered to remove variability at timescales longer than 7 years[1]. The modern coral $\delta^{18}O$ anomaly and the instrumental DMI anomaly during the July–December IOD season have similarly significant correlations ($r = 0.79$, $P < 0.01$, $n_{eff} = 14$; 1982–2000).

Positive IOD events in the DMI and modern coral $\delta^{18}O$ anomaly records are detected using a threshold exceedance method, relative to the standard deviation ($\sigma$) of variability during their 1961–1990 climatological reference intervals (Methods). This event detection method identifies known positive IOD events in instrumental datasets, including the extreme positive IOD events of 1961, 1994, 1997 and 2019 (Fig. 1c)[1,18]. Notably, the three-in-a-row event[13] previously reported for 2006, 2007 and 2008 is now detected only as a single large event in 2006, suggesting that earlier detection was biased by decadal-scale variability and trends in Indian Ocean SST rather than reflecting true consecutive occurrences of positive IOD events. The same event detection methodology and 1961–1990 modern coral reference interval is used to characterize IOD behaviour during the last millennium from the fossil coral records.

## Last millennium IOD reconstruction

The fossil coral reconstruction of IOD variability during the last millennium follows the approach used in the central Pacific to reconstruct floating time windows of ENSO variability[21]. Eight fossil coral records from the southern Mentawai Islands are used to reconstruct monthly-resolved IOD variability (Extended Data Fig. 4; Supplementary Table 1). Internal chronologies were constructed by tying the annual $\delta^{18}O$ maximum to the month of the climatological SST minima (October; see Methods). Precise U–Th dating, typically with $2\sigma$ errors less than ±15 years (Supplementary Table 2), and characteristic patterns of interannual variability allow time-overlapping fossil corals to be accurately spliced together to form longer climate sequences[21] (Methods). The consistent pattern and magnitude of mean annual $\delta^{18}O$ cycles in the fossil coral records, and the strong correspondence of interannual $\delta^{18}O$ variability in overlapping fossil coral sections, indicates that there are no site-specific biases in the coral representations of climate signals (Extended Data Fig. 4c; Supplementary Figs. 12, 14–16). When combined with instrumental records of recent IOD variability, and the previously published modern coral DMI reconstruction, the spliced fossil coral data allow IOD variability to be assessed across 500 years since 1240 (Fig. 2; Methods).

Positive IOD events are detected throughout the last millennium reconstruction, but extreme positive IOD events were rare before 1960 (Fig. 2). Prior to this time, just six events exceeding the $3\sigma$ extreme event detection level occur in the IOD reconstruction (Extended Data Figs 5 and 6). This extended perspective across the last millennium strengthens earlier findings that positive IOD events have become more intense in recent decades[5] and that extreme positive IOD events are projected to become more common with greenhouse warming[6].

The reconstruction also demonstrates, however, that the strongest event in modern times was not unprecedented. During the peak of the extreme 1997 event, monthly mean SST and rainfall anomalies in the southern Mentawai Islands reached −3.5 °C and −7.0 mm per day,

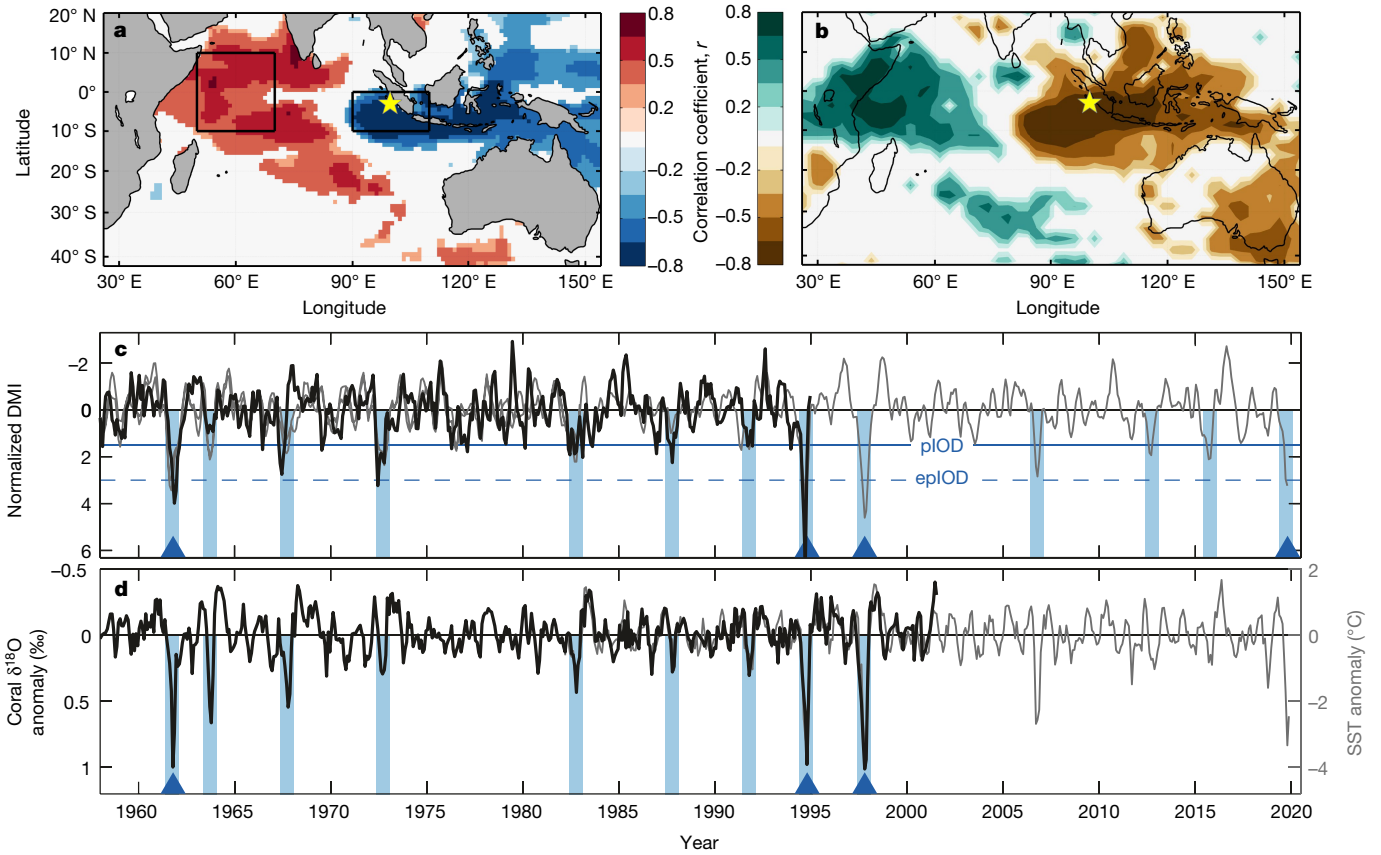


**Fig. 1 | IOD variability in the southern Mentawai Islands. a**, **b**, The study area (3° S, 100° E; yellow stars) lies within the region of maximum correlation of SST (**a**) and rainfall (**b**) with the DMI. The DMI is defined[1] as the west–east difference in SST anomalies in the two regions indicated by black boxes in **a**. Correlations are for July–December means, shown by shading where $P < 0.1$. **c**, Instrumental SST (thin grey) and coral-derived (thick black) records of the DMI, normalized relative to 1961–1990 after removing variability at timescales longer than 7 years. Positive IOD events (pIOD; exceeding $+1.5\sigma$) are denoted by blue shading, and extreme positive IOD events by blue triangles (epIOD; exceeding $+3\sigma$; Methods). **d**, Coral $\delta^{18}O$ (black; inverted *y* axis) and instrumental SST (grey) anomalies from the study site document prominent cool and dry anomalies during positive IOD events. This study site has been previously shown to be the optimum site for reconstructing the occurrence and magnitude of positive IOD events[18]. Anomalies were calculated by removing variability at timescales longer than 7 years.

respectively. These extreme cool and dry conditions were recorded in coral $\delta^{18}O$ as a monthly mean anomaly of 1.01 ± 0.01‰ (standard error of the mean; see Methods and Extended Data Fig. 6). In the IOD reconstruction an even larger extreme positive IOD event occurred in 1675. The maximum $\delta^{18}O$ anomaly for this prehistoric extreme positive IOD event was 1.29 ± 0.01‰ (Methods), indicating that the maximum intensity of this event was about 27% larger than the 1997 event. This difference is even greater when assessed across the full IOD season, with the mean July–December $\delta^{18}O$ anomaly of the 1675 event 42% larger than in 1997 (Extended Data Fig. 6).

The extreme 1675 event does not appear to be related to external climate forcing. This event occurred well before the onset of anthropogenic climate warming[22], and although climate model simulations suggest that volcanic eruptions could promote the development of positive IOD events[23] (Supplementary Fig. 22), the 1675 event occurred during an interval with no major volcanic eruptions[24]. The extreme event documented in this same coral in 1660 (Extended Data Fig. 6c) coincided with a very strong El Niño event in 1660/61 (refs. [25,26]), and historical documents from Indonesia describe 1660 as being a year of unprecedented drought across the entire Indonesian archipelago that led to widespread famine and mortality[27]. Historical documents also describe extreme drought and famine in Indonesia in 1675, which was exacerbated by simultaneous failures of rice crops in India and Thailand and incited war in Java across the 1674–79 period[27]. In this case, there does not appear to be any historical evidence for a strong El Niño event in any of the years around 1675 that may have promoted the development of this extreme positive IOD event[25,26]. The 1675 event provides evidence that even the most extreme IOD variability can apparently arise from natural variability within the Indian Ocean without the need for external forcing.

The seventeenth century stands out as an interval of unusually high variability in the last millennium IOD reconstruction. Moving 30-year standard deviations of July–December averaged $\delta^{18}O$ anomalies show that IOD variability was near to or less than that of the 1961–1990 reference interval for much of the last millennium, apart from the seventeenth century and recent decades (Fig. 2). During the seventeenth century, variability of the IOD was on average 55% greater than during 1961–1990. This unusually high variability is in part related to the 1675 extreme positive IOD event. However, even if the $\delta^{18}O$ magnitude of this event is capped at the level of the 1997 extreme event, the seventeenth century still stands out as an extended period when IOD variability was consistently higher (by around 32%) than during 1961–1990. Therefore, it appears that intensification of the IOD in recent decades is not yet outside the range of natural variability experienced during the last millennium.

## Tropical Indo-Pacific coupling

Emerging knowledge suggests that tropical climate variability interacts across ocean basins, but short observational records limit the ability to clearly define and understand these interactions across the full range of interannual to multi-decadal timescales[8]. Here we test the coherency of

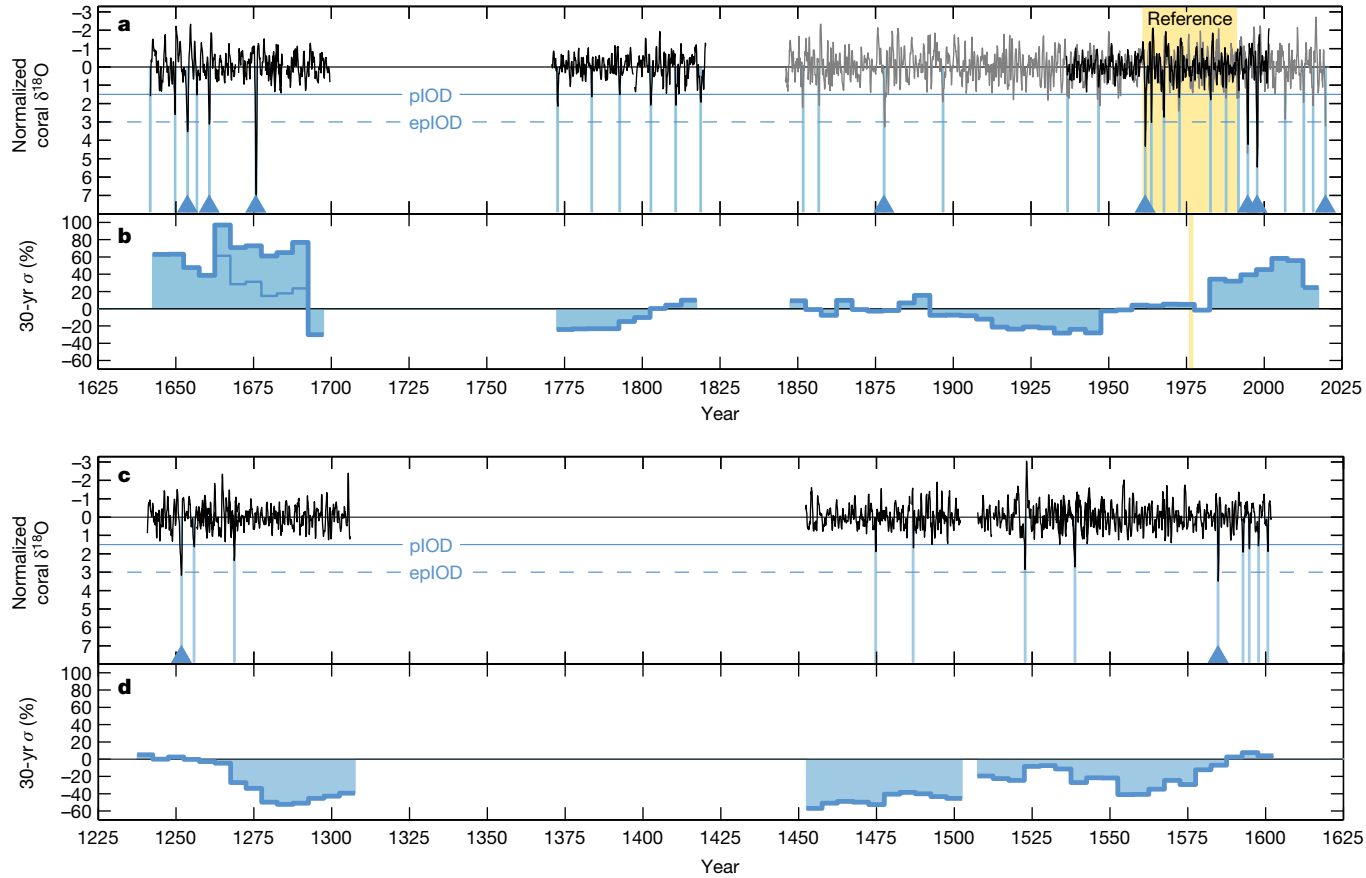


**Fig. 2 | The IOD during the last millennium. a**, **c**, The last millennium IOD reconstruction is derived from nine southern Mentawai Island coral $\delta^{18}O$ records (black), and the DMI from instrumental data and a previously published coral-based reconstruction[5] (grey). All records are normalized relative to 1961–1990 variability (Methods). The occurrence of pIOD (blue shading) and epIOD (blue triangles) events during the last millennium is also shown. **b**, **d**, Standard deviation $\sigma$ of July–December means of IOD variability in moving 30-year windows stepped by 5 years, expressed as a percentage change relative to the 1961–1990 reference interval. The thin line for the 30-year interval centred around 1675 gives the moving standard deviation if the strength of the extreme 1675 event is capped at the magnitude of the $\delta^{18}O$ anomaly for the strongest-on-record 1997 event.

interannual variability between the tropical Indian and Pacific oceans by comparing the IOD reconstruction with an analogous coral-based reconstruction of ENSO variability during the last millennium from the Line Islands in the central Pacific[21,28,29]. The coral-based ENSO reconstruction is sensitive to El Niño variability related to central-Pacific and eastern-Pacific type events (Supplementary Table 3), and has been used to demonstrate that interannual (2–7 year) variability in the central tropical Pacific shows a wide range of unforced internal variability[21,28,29]. These studies conclude that late-twentieth-century ENSO variance is significantly ($P < 0.05$) stronger than in the pre-industrial era, but not yet unprecedented.

The coral-based IOD and ENSO reconstructions demonstrate a remarkable coherency between the interannual variability of the two tropical ocean basins (Fig. 3). Changes in interannual ENSO and IOD variability during the last millennium have comparable timing and magnitude in the moving 30-year standard deviations of both datasets. Notably, the only interval of the last millennium showing higher ENSO variability than the twentieth century is the mid-seventeenth century[21], and this corresponds to the same interval of elevated variability identified in the IOD reconstruction. Correlation analysis indicates that approximately 45% of the magnitude of interannual variability is shared between the IOD and ENSO systems during the last millennium ($r = 0.67$, $n_{eff} = 14$, $P < 0.01$; Fig. 3c). This increases to 60% shared variance if the magnitude of the extreme 1675 event is capped at the $\delta^{18}O$ anomaly of the 1997 event ($r = 0.77$, $n_{eff} = 14$, $P < 0.01$). The tight coupling of IOD and ENSO variability across the coral reconstructions does not imply that IOD events can only occur in conjunction with El Niño events (for example, the 2019, 1961 and 1675 events demonstrate that even extreme IOD events can occur independently of El Niño conditions in the Pacific). It does, however, provide a long-term context that supports hypotheses of tropical Indo-Pacific climate coupling based on observational data[8,30], and suggests that the coral-based IOD and central-Pacific ENSO datasets can be used together as a near-continuous representation of tropical Indo-Pacific interannual variability through the last millennium (Fig. 3b).

Long-term modulation of IOD–ENSO variability appears to have been accompanied by changes in the mean SST gradient across the equatorial Pacific (Fig. 3d). Previous assessments of marine sediment cores identified a mid-millennium shift in tropical Pacific climate, from a state with dampened ENSO variability and a strong zonal SST gradient during the first half of the last millennium, to one with amplified ENSO variability and a weak zonal SST gradient in the latter half[31]. The high-resolution coral reconstructions support this finding, and add to it by demonstrating that a statistically significant transition in IOD–ENSO variability occurred in approximately 1590 (Fig. 3b; Extended Data Fig. 7). Prior to 1590, variability of the IOD was on average 29% lower than during the 1961–1990 reference interval, and ENSO variability was similarly reduced by 30%. This tropical climate transition is also evident in the frequency of positive IOD events, which display a threefold increase in occurrence after the mid-millennium shift; having a mean periodicity of 25 years before 1590, and 8 years after 1590 (Fig. 2).

Changes in the strength of IOD–ENSO variability, including the mid-millennium shift, may affect the ability to reconstruct these climate modes reliably in the past using remote proxies that rely on a

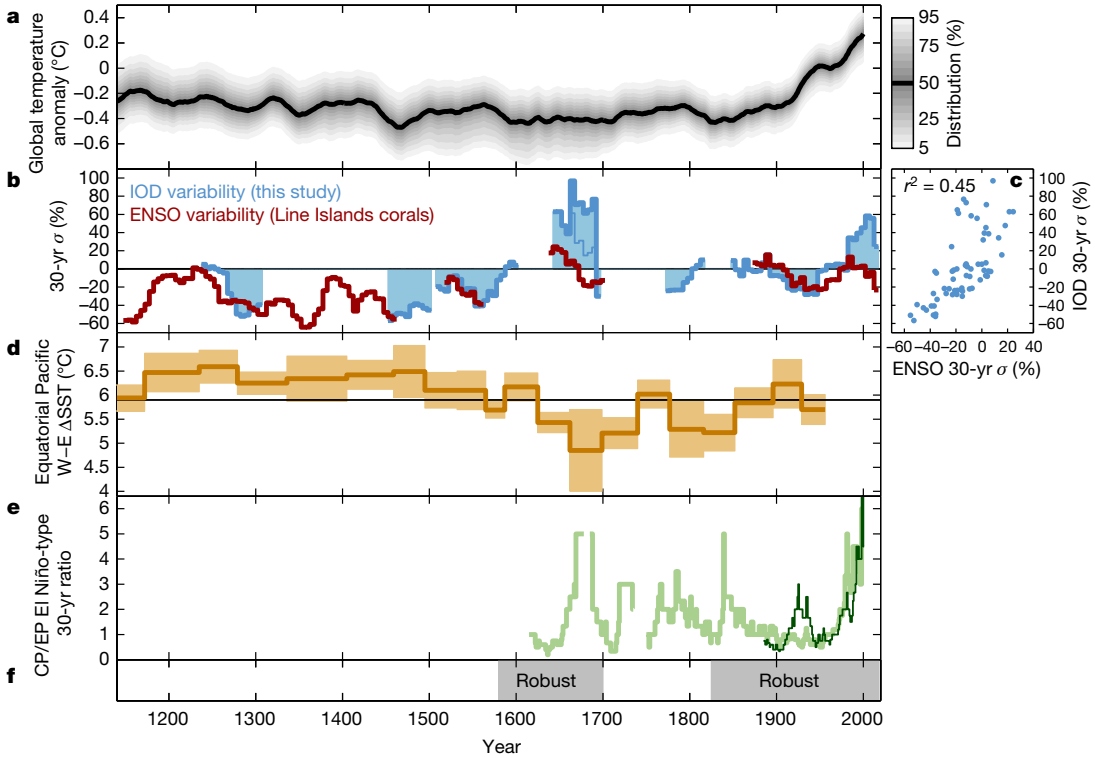


**Fig. 3 | Coupled Indo-Pacific climate variability during the last millennium.** **a**, Global mean surface temperature anomalies[50] for the last millennium, relative to 1961–1990 and plotted as 30-year moving averages with shading giving the distribution across 7,000 reconstructions. **b**, Moving 30-year standard deviations, stepped by 5 years, of coral-based IOD (blue) and ENSO (red)[21,28,29] variability, expressed as percentage change relative to their 1961–1990 reference intervals. **c**, Scatter plot of 30-year variability of the coral-based IOD and ENSO reconstructions for coeval data during the last millennium, demonstrating strong coupling in Indo-Pacific variability ($P < 0.01$). The coral IOD and ENSO data support a significant ($P < 0.05$) mid-millennium shift in tropical climate variability around 1590 (Extended Data Fig. 7) that is also evident in changes in the west–east SST gradient across the equatorial Pacific reconstructed from marine sediments[31] (**d**). **e**, Anomalous IOD and ENSO conditions in the seventeenth century also include an unusual increase in the ratio of central-Pacific-type to eastern-Pacific-type El Niño events (CP/EP) (reconstructed in light green, observed (HadISST) in dark green)[33]. **f**, Robust agreement[32] between ENSO reconstructions derived from teleconnected climate patterns coincide with strengthening of IOD–ENSO variability after approximately 1590.

teleconnected signal. Agreement between interannual ENSO reconstructions derived from teleconnected (and often hydroclimate-related) anomalies is poor for most of the last millennium, but is most robust for 1580–1700 and from 1825 onwards[32]. These intervals of agreement correspond to times when the coral reconstructions indicate that interannual IOD–ENSO variability was relatively strong (greater than, or no more than about 20% reduced, relative to the 1961–1990 reference levels; Fig. 3b, f). Disagreement between reconstructions at other times suggests that it may be difficult to robustly reconstruct interannual tropical climate variability from teleconnected signals when variability itself is low.

There is widespread agreement among proxy evidence that the most extreme variability and mean-state shifts in tropical Indo-Pacific climate occurred around the seventeenth century. During this interval, when the highest variability in IOD and ENSO of the last millennium is recorded, the most reduced zonal SST gradient also existed across the equatorial Pacific (Fig. 3d). A recent reconstruction of El Niño event types, based on patterns of seasonal evolution in coral data, also identified the seventeenth century as an interval of unusually frequent central-Pacific-type events[33] (Fig. 3e). Across the Indian Ocean, peak cooling in Indo-Pacific Warm Pool SST around the seventeenth century was simultaneous with the timing of maximum rainfall in eastern Africa, and suggestive of a positive IOD-like mean state with reduced zonal SST gradient and weakened Walker circulation across the Indian Ocean[34]. Coral evidence suggests that the summer and winter Asian monsoon winds were also highly variable on interannual timescales during the seventeenth century[35]. The Asian and Australian summer monsoons both experienced their driest mean conditions of the last millennium during the seventeenth century, resulting in a strong latitudinal contraction and intensification of the tropical rainfall belt over the Indo-Pacific Warm Pool[36,37] despite cool SSTs in the region at this time[31,34]. The strong East Asian winter monsoon during the seventeenth century[38] may provide a mechanism for enhanced atmospheric convergence and rainfall over the Indo-Pacific Warm Pool[39] at a time when SST gradients indicate a more El Niño-like zonal mean state across the Pacific[31]. The seventeenth century is known as an interval of crisis in tropical Asia, involving widespread mortality and economic and political disruption[26,27]. This upheaval has been attributed to strong El Niño variability[26] and a weak Asian summer monsoon[38,40], but our coral-based reconstruction suggests that unusually strong variability of the IOD was also a factor in causing societal disruption across Asia during the seventeenth century.

## Data–model comparison

We explore the coupling of tropical Indian and Pacific Ocean variability further using the Community Earth System Model (CESM1) Last Millennium Ensemble (LME)[41]. The CESM1-LME full-forcing simulations replicate the spatial structure of SST and rainfall anomalies associated with the IOD (Extended Data Fig. 2), and the characteristic skewness of IOD variability (Supplementary Fig. 18). However, important differences are seen in the recurrence interval of positive IOD events in the CESM1 output compared with the coral-based reconstruction (Extended Data Fig. 8). The most common recurrence time between positive IOD events

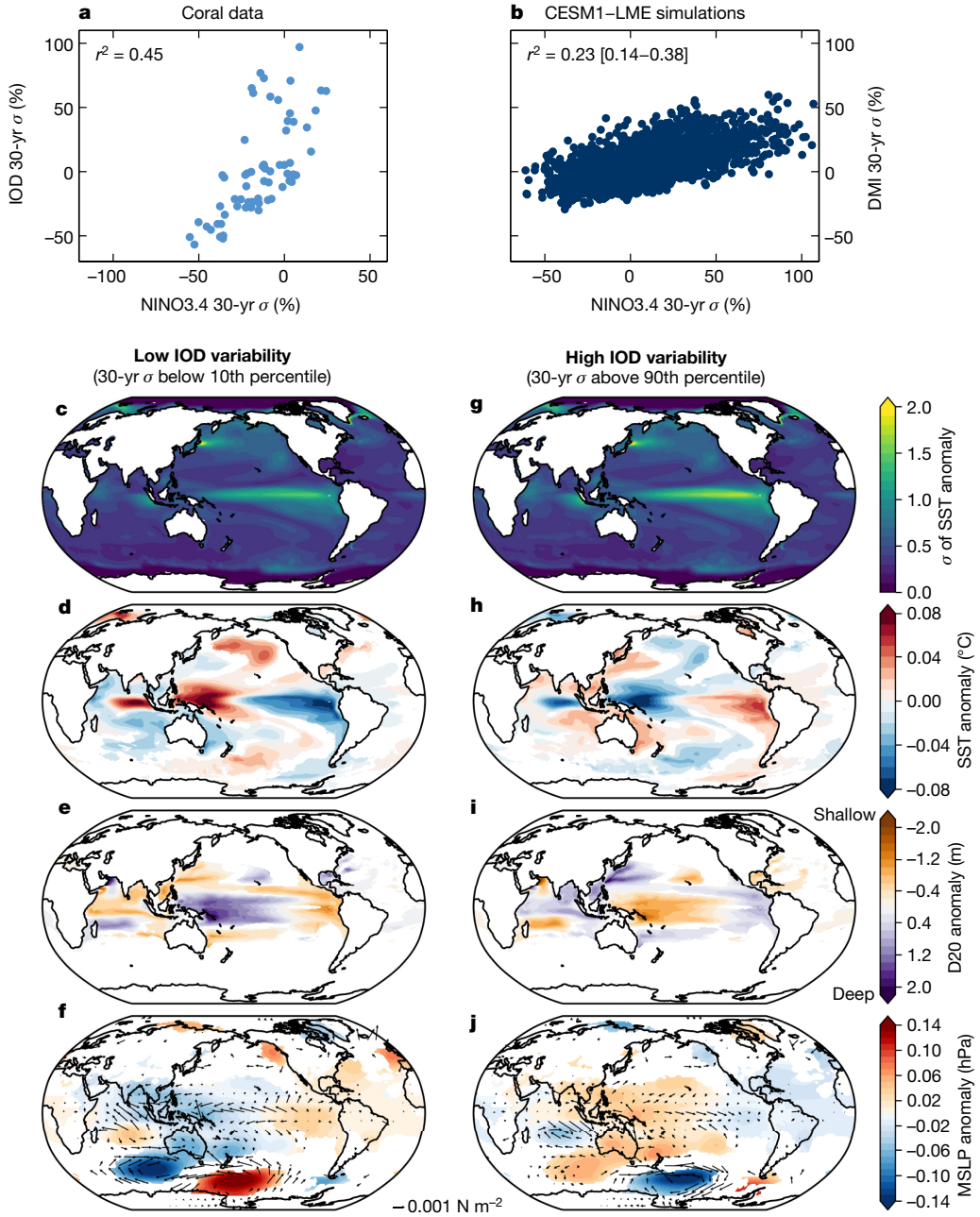


**Fig. 4 | Coupling of IOD–ENSO variability in last millennium simulations.** **a**, Scatter plot of 30-year standard deviations of reconstructed IOD and ENSO variability, expressed as percentage change relative to 1961–1990 (as in Fig. 3c); **b**, the equivalent analysis using the DMI and NINO3.4 indices extracted from the CESM1-LME simulations, demonstrating a persistent coupling of IOD–ENSO variability during the last millennium. **c**–**f**, Composite maps of the standard deviation $\sigma$ of July–December SST anomalies (**c**), and the July–December averages of anomalies of SST (**d**), depth of the 20 °C isotherm (D20) (**e**), and mean sea level pressure (MSLP; shading) and surface wind stress (arrows) (**f**), calculated across all 30-year intervals where July–December IOD variability was below the 10th percentile in the CESM1-LME full forcing ensemble. **g**–**j**, As in **c**–**f**, but composited across all 30-year intervals where IOD variability was above the 90th percentile. All linear correlations in **a** and **b** are significant at $P < 0.01$, and data are shown in **c**–**j** only for grid cells where distributions between intervals of low and high IOD variability are significantly ($P < 0.05$) different based on a Kolmogorov–Smirnov test.

is 1 year in the CESM1-LME, but back-to-back positive IOD events are not observed in the coral reconstruction. This difference is consistent with other studies that have noted a bias for positive IOD events to occur too frequently in historical simulations of current-generation climate models[7]. Nevertheless, the CESM1-LME simulations are still useful to identify possible mechanisms and teleconnections associated with the IOD–ENSO coupling observed in last millennium coral data.

Coupling of the magnitude of interannual IOD and ENSO variability is a persistent feature of the last millennium in the CESM1-LME experiments (Fig. 4a, b). Across all full-forcing ensemble members there is 23% shared variance, ranging from 14% to 38% in individual ensemble members (Fig. 4b; $P < 0.01$ for all members). We explore this further by constructing composites of intervals of high and low IOD variability, based on time intervals where the 30-year standard deviation of the July–December DMI is above the 90th percentile and below the 10th percentile, respectively (Fig. 4c–j; Extended Data Fig. 9). The composite anomalies suggest that intervals of low IOD variability are associated with low SST variability in the NINO3.4 region and a La Niña-like pattern in mean tropical Pacific SSTs (consistent with the palaeo-evidence; see Fig. 3), as well as a deep thermocline and low surface air pressure

anomalies in the Indo-Pacific Warm Pool region. Conversely, intervals of high IOD variability are associated with high SST variability in the NINO3.4 region and El-Niño-like mean SST anomalies, and ocean–atmosphere conditions in the Indo-Pacific Warm Pool region that are conducive to the development of positive IOD events (for example, high surface air pressure and shallow thermocline anomalies).

Simulated mean SST anomalies in the composites of low and high IOD variability display an equatorial extension of anomalies from the eastern Indian Ocean into the central Indian Ocean (Fig. 4d, h; Extended Data Fig. 9b, f). Extension of anomalies into the central equatorial Indian Ocean has been observed during recent extreme positive IOD events[6], and this characteristic has also been seen in CESM1 simulations for the Last Glacial Maximum indicating the potential for strengthened ocean–atmosphere coupling in the tropical Indian Ocean that enhances SST variability[42]. The composites of atmospheric pressure (Fig. 4f, j; Extended Data Fig. 9d, h) also display distinct Rossby wave trains originating in the tropical Indian Ocean and travelling across Australia and the Southern Ocean to the Amundsen Sea and Antarctic Peninsula region. It is possible that the tight coupling of tropical Indian Ocean climate variability to the Pacific may be important, via this wave train mechanism, in the recently identified connection between the tropical Indian and Pacific oceans and climate variability in the West Antarctic region[43,44].

We also explore mechanisms for decadal-scale modulation of positive IOD event recurrence by constructing composites of the CESM1-LME simulations based on decades with frequent (4 or more) or rare (1 or less) positive IOD events (Extended Data Fig. 10). As expected, composites of decades with frequent positive IOD events are characterized by a mean positive-IOD-like state in the tropical Indian Ocean related to the averaging of a large number of positive IOD events together. However, the anomaly patterns also show a coherent ocean–atmosphere structure extending across the tropical and extratropical Pacific that resembles Interdecadal Pacific Oscillation variability[45]. This relationship in the CESM1-LME simulations is further confirmed through the significant relationship that exists between indices of the IOD and the Interdecadal Pacific Oscillation (47% shared variance; $P < 0.01$; Extended Data Fig. 10). Clustering of positive IOD events has been observed in the instrumental record and linked to decadal variability in the Pacific that causes intervals of a shallower thermocline in the eastern equatorial Indian Ocean that preconditions the development of positive IOD events[46,47]. Decadal to multi-decadal modulation between intervals of frequent and rare positive IOD events is also a characteristic of the coral reconstruction of IOD variability during the last millennium (Fig. 2; Extended Data Fig. 8a).

## Implications for managing climate risk

Our new reconstruction of IOD variability during the last millennium has implications for managing the climate risks associated with tropical climate variability. In particular, the reconstruction demonstrates that the extreme conditions that occurred in the tropical Indian Ocean during 1997 are not the worst that are possible. Positive IOD events larger than the 1997 event are also known from the mid-Holocene when background climate conditions were different from today[11,48], but the discovery of a similarly extreme positive IOD event from the last millennium with no obvious external forcing indicates that present-day IOD risk management needs to include the possibility of severe events beyond what is known from the instrumental record. This is of particular concern when viewed alongside model-based evidence of an increasing occurrence of extreme positive IOD events with continued climate warming[6].

Clustering of positive IOD events may mean that there is potential for skilful seasonal-to-decadal forecasting of the climate risks posed by the IOD. The mechanisms by which decadal variability modulates the IOD are still poorly understood[4], but the tropical Indian Ocean is a region where skilful decadal prediction could be most viable[49]. However, the risk of back-to-back IOD events is overestimated in current-generation climate models[7] (Extended Data Fig. 8), and the low number of events in observational data make it difficult to establish statistical estimates of IOD event risk. The extended context provided by the last millennium IOD reconstruction compiled here demonstrates that the most common recurrence interval between positive IOD events is 3 years, consistent with the phasing of the 1994–1997 sequence, and that recurrent events frequently occur within the 2- to 6-year window following a positive event (Extended Data Figs. 5, 8a). Statistically, in the last millennium reconstruction there is a 47% probability (with a 95% confidence interval of 31–63%) that a positive IOD event will recur within 2 to 6 years of another positive event (Extended Data Fig. 8c). The tight coupling of IOD and ENSO variability during the last millennium identified in this study also suggests that efforts to develop skilful seasonal to decadal forecasting will be aided by realistic model representation of the coherent climate interactions that occur across the Indo-Pacific region[8,30]. Together, the evidence gathered here on tropical Indo-Pacific climate variability has the potential to aid societal adaptation to future impacts of the IOD.

## Online content

Any methods, additional references, Nature Research reporting summaries, source data, extended data, supplementary information, acknowledgements, peer review information; details of author contributions and competing interests; and statements of data and code availability are available at https://doi.org/10.1038/s41586-020-2084-4.


1. Saji, N. H., Goswami, B. N., Vinayachandran, P. N. & Yamagata, T. A dipole mode in the tropical Indian Ocean. *Nature* **401**, 360–363 (1999).
2. Webster, P. J., Moore, A. M., Loschnigg, J. P. & Leben, R. R. Coupled ocean–atmosphere dynamics in the Indian Ocean during 1997–98. *Nature* **401**, 356–360 (1999).
3. Cai, W. et al. Projected response of the Indian Ocean Dipole to greenhouse warming. *Nat. Geosci.* **6**, 999–1007 (2013).
4. Han, W. et al. Indian Ocean decadal variability: a review. *Bull. Am. Meteorol. Soc.* **95**, 1679–1703 (2014).
5. Abram, N. J., Gagan, M. K., Cole, J. E., Hantoro, W. S. & Mudelsee, M. Recent intensification of tropical climate variability in the Indian Ocean. *Nat. Geosci.* **1**, 849–853 (2008).
6. Cai, W. et al. Increased frequency of extreme Indian Ocean Dipole events due to greenhouse warming. *Nature* **510**, 254–258 (2014).
7. Weller, E. & Cai, W. Realism of the Indian Ocean Dipole in CMIP5 models: the implications for climate projections. *J. Clim.* **26**, 6649–6659 (2013).
8. Cai, W. et al. Pantropical climate interactions. *Science* **363**, eaav4236 (2019).
9. Ummenhofer, C. C. et al. What causes southeast Australia's worst droughts? *Geophys. Res. Lett.* **36**, L04706 (2009).
10. Cai, W., Cowan, T. & Raupach, M. Positive Indian Ocean Dipole events precondition southeast Australia bushfires. *Geophys. Res. Lett.* **36**, (2009).
11. Abram, N. J., Gagan, M. K., McCulloch, M. T., Chappell, J. & Hantoro, W. S. Coral reef death during the 1997 Indian Ocean dipole linked to Indonesian wildfires. *Science* **301**, 952–955 (2003).
12. Hashizume, M., Chaves, L. F. & Minakawa, N. Indian Ocean Dipole drives malaria resurgence in East African highlands. *Sci. Rep.* **2**, 269 (2012).
13. Cai, W., Sullivan, A. & Cowan, T. Climate change contributes to more frequent consecutive positive Indian Ocean Dipole events. *Geophys. Res. Lett.* **36**, L23704 (2009).
14. Cai, W. et al. Stabilised frequency of extreme positive Indian Ocean Dipole under 1.5 °C warming. *Nat. Commun.* **9**, 1419 (2018).
15. Stevenson, S., Fox-Kemper, B., Jochum, M., Rajagopalan, B. & Yeager, S. G. ENSO model validation using wavelet probability analysis. *J. Clim.* **23**, 5540–5547 (2010).
16. Wittenberg, A. T. Are historical records sufficient to constrain ENSO simulations? *Geophys. Res. Lett.* **36**, L12702 (2009).
17. Meyers, G., McIntosh, P., Pigot, L. & Pook, M. The years of El Niño, La Niña, and interactions with the tropical Indian Ocean. *J. Clim.* **20**, 2872–2880 (2007).
18. Abram, N. J. et al. Optimized coral reconstructions of the Indian Ocean Dipole: an assessment of location and length considerations. *Paleoceanography* **30**, 1391–1405 (2015).
19. Thompson, D. M., Ault, T. R., Evans, M. N., Cole, J. E. & Emile-Geay, J. Comparison of observed and simulated tropical climate trends using a forward model of coral $\delta^{18}O$. *Geophys. Res. Lett.* **38**, L14706 (2011); correction **38**, L19705 (2011).
20. Konecky, B. L., Noone, D. C. & Cobb, K. M. The influence of competing hydroclimate processes on stable isotope ratios in tropical rainfall. *Geophys. Res. Lett.* **46**, 1622–1633 (2019).
21. Cobb, K. M., Charles, C. D., Cheng, H. & Edwards, R. L. El Nino/Southern Oscillation and tropical Pacific climate during the last millennium. *Nature* **424**, 271–276 (2003).
22. Abram, N. J. et al. Early onset of industrial-era warming across the oceans and continents. *Nature* **536**, 411–418 (2016).

23. Maher, N., McGregor, S., England, M. H. & Gupta, A. S. Effects of volcanism on tropical variability. *Geophys. Res. Lett.* **42**, 6024–6033 (2015).
24. Sigl, M. et al. Timing and climate forcing of volcanic eruptions for the past 2,500 years. *Nature* **523**, 543–549 (2015).
25. Gergis, J. L. & Fowler, A. M. A history of ENSO events since A.D. 1525: implications for future climate change. *Clim. Change* **92**, 343–387 (2009).
26. Grove, R. & Adamson, G. in *El Niño in World History* (eds Grove, R. & Adamson, G.) 49–79 (Palgrave Macmillan, 2018).
27. Boomgaard, P. in *Asian Population History* (eds Liu, T. et al.) 451 (Oxford Univ. Press, 2001).
28. Cobb, K. M. et al. Highly variable El Nino/Southern Oscillation throughout the Holocene. *Science* **339**, 67–70 (2013).
29. Grothe, P. R. et al. Enhanced El Niño-Southern Oscillation variability in recent decades. *Geophys. Res. Lett.* **46**, https://doi.org/10.1029/2019GL083906 (2019).
30. Stuecker, M. F. et al. Revisiting ENSO/Indian Ocean Dipole phase relationships. *Geophys. Res. Lett.* **44**, 2481–2492 (2017).
31. Rustic, G. T., Koutavas, A., Marchitto, T. M. & Linsley, B. K. Dynamical excitation of the tropical Pacific Ocean and ENSO variability by Little Ice Age cooling. *Science* **350**, 1537–1541 (2015).
32. Dätwyler, C., Abram, N. J., Grosjean, M., Wahl, E. R. & Neukom, R. El Niño–Southern Oscillation variability, teleconnection changes and responses to large volcanic eruptions since AD 1000. *Int. J. Clim.* **39**, 2711–2724 (2019).
33. Freund, M. B. et al. Higher frequency of Central Pacific El Nino events in recent decades relative to past centuries. *Nat. Geosci.* **12**, 450–455 (2019).
34. Tierney, J. E., Smerdon, J. E., Anchukaitis, K. J. & Seager, R. Multidecadal variability in East African hydroclimate controlled by the Indian Ocean. *Nature* **493**, 389–392 (2013).
35. Goodkin, N. F. et al. East Asian monsoon variability since the sixteenth century. *Geophys. Res. Lett.* **46**, 4790–4798 (2019).
36. Denniston, R. F. et al. Expansion and contraction of the Indo-Pacific tropical rain belt over the last three millennia. *Sci. Rep.* **6**, 34485 (2016).
37. Yan, H. et al. Dynamics of the intertropical convergence zone over the western Pacific during the Little Ice Age. *Nat. Geosci.* **8**, 315 (2015).
38. Yancheva, G. et al. Influence of the intertropical convergence zone on the East Asian monsoon. *Nature* **445**, 74–77 (2007).
39. Ma, T. et al. East Asian winter monsoon impacts the ENSO-related teleconnections and North American seasonal air temperature prediction. *Sci. Rep.* **8**, 6547 (2018).
40. Zhang, P. et al. A test of climate, sun, and culture relationships from an 1810-year Chinese cave record. *Science* **322**, 940–942 (2008).
41. Otto-Bliesner, B. L. et al. Climate variability and change since 850 CE: an ensemble approach with the Community Earth System Model. *Bull. Am. Meteorol. Soc.* **97**, 735–754 (2016).
42. Thirumalai, K., DiNezio, P. N., Tierney, J. E., Puy, M. & Mohtadi, M. An El Niño mode in the glacial Indian Ocean? Paleoceanogr. *Paleoclimatol.* **34**, 1316–1327 (2019).
43. Holland, P. R., Bracegirdle, T. J., Dutrieux, P., Jenkins, A. & Steig, E. J. West Antarctic ice loss influenced by internal climate variability and anthropogenic forcing. *Nat. Geosci.* **12**, 718–724 (2019).
44. Purich, A. & England, M. H. Tropical teleconnections to Antarctic sea ice during austral spring 2016 in coupled pacemaker experiments. *Geophys. Res. Lett.* **46**, 6848–6858 (2019).
45. Henley, B. J. et al. A tripole index for the Interdecadal Pacific Oscillation. *Clim. Dyn.* **45**, 3077 (2015).
46. Ummenhofer, C. C., Biastoch, A. & Böning, C. W. Multidecadal Indian Ocean variability linked to the Pacific and implications for preconditioning Indian Ocean Dipole events. *J. Clim.* **30**, 1739–1751 (2017).
47. Zhang, L., Du, Y. & Cai, W. Low-frequency variability and the unusual Indian Ocean Dipole events in 2015 and 2016. *Geophys. Res. Lett.* **45**, 1040–1048 (2018).
48. Abram, N. J. et al. Seasonal characteristics of the Indian Ocean Dipole during the Holocene epoch. *Nature* **445**, 299–302 (2007).
49. Guemas, V. et al. The Indian Ocean: the region of highest skill worldwide in decadal climate prediction. *J. Clim.* **26**, 726–739 (2013).
50. PAGES 2K Consortium. Global multi-decadal variability in global temperature reconstructions and simulations over the Common Era. *Nat. Geosci.* **12**, 643–649 (2019).

# Methods

### Study site

The coral samples used in this study come from the southern Mentawai Islands, spanning from South Pagai Island to Sipora Island (Extended Data Fig. 1, Supplementary Fig. 1). A location of 3° S and 100° E is used to extract local SST and precipitation data from observational products. The grid cell incorporating 3° S and 100° E is also used to extract site-level SST and precipitation output from the CESM1-LME simulations.

The mean annual SST range at the study site is 1.3 °C, with a monthly mean minimum of 28.6 °C (25–75% range of 28.6 °C to 29.1 °C) in October, and a monthly mean maximum of 29.9 °C (25–75% range of 29.7 °C to 30.1 °C) in May (OISSTv2)[51]. The monthly mean minimum rainfall of 5.7 mm per day (25–75% range of 4.3 mm per day to 6.8 mm per day) occurs in May, and the monthly mean maximum of 11.2 mm per day (25–75% range of 9.2 mm per day to 12.8 mm per day) occurs in November (GPCPv2.3)[52].

Tectonic activity in the Mentawai Islands is characterized by multi-century supercycles of long-term subsidence, typically on the order of 3–15 mm per year, followed by rapid uplift (earthquake) events[53]. Any effect of long-term subsidence on geochemistry of the Mentawai corals is expected to be partially or wholly offset by the effects of upward colony growth.

### Coral sampling and analysis

Drill cores from modern and fossil *Porites* corals were collected from the southern Mentawai Islands in 2001, and well preserved samples that covered the last millennium were selected for analysis in this study. In addition, a *Porites* coral microatoll slab sampled in 1994 (refs. [54,55]) is included in our reconstruction of IOD variability during the last millennium. Details of sample location, length, preservation and age are given in Supplementary Tables 1 and 2.

Coral cores were cut along their length to give slabs approximately 7 mm thick, which were X-rayed to identify coral growth layers (Supplementary Figs. 2–9). Slabs were cut adjacent to sampling transects selected along the major coral growth axis, and the sampling edge was milled to reduce the slab thickness to ~3.5 mm (Supplementary Fig. 10). The resulting sampling edge was cleaned thoroughly in deionized water under an ultrasonic probe before being dried in an oven at 40 °C for at least 48 hours.

Diagenesis checks were carried out using a combination of visual examination and X-ray images of the coral slabs. Further checks were carried out using thin sections made from coral slab offcuts produced during preparation of sampling edges. Thin sections demonstrate good to excellent preservation of all coral samples used in this study[56] (Supplementary Fig. 11).

Subsamples of coral powder were milled continuously along the edge of the sampling transects, generally at 0.4 mm resolution (Supplementary Figs. 2–9). Coral powders were weighed and analysed for their $\delta^{18}O$ and $\delta^{13}C$ composition using a Finnigan MAT-251 isotope ratio mass spectrometer coupled to a Kiel I carbonate device (using 180–220 μg samples), or a Thermo MAT-253 isotope ratio mass spectrometer coupled to a Kiel IV carbonate device (using 110–130 μg samples), at the Research School of Earth Sciences at the Australian National University. Analyses were calibrated using the International Atomic Energy Agency (IAEA) NBS-19 standard ($\delta^{18}O_{VPDB} = -2.20‰$ and $\delta^{13}C_{VPDB} = 1.95‰$; VPBD, Vienna Pee-Dee Belemnite standard). A further linear correction for $\delta^{18}O$ measurements was carried out using the IAEA NBS-18 standard ($\delta^{18}O_{VPDB} = -23.0‰$; we note that the old NBS-18 IAEA reference value is used to maintain consistency of results across the Australian National University Stable Isotope Facility). Long-term precision of both the MAT-251 and MAT-253 instruments is ±0.06‰ for $\delta^{18}O$ and ±0.04‰ for $\delta^{13}C$.

This study uses 6,630 analyses of coral powders to reconstruct IOD variability during the last millennium. Across these measurements, the standard deviation of reproducibility on 1,198 replicate analyses of coral powder samples is ±0.05‰ for $\delta^{18}O$ and ±0.10‰ for $\delta^{13}C$.

### Coral chronologies

Internal chronologies for the coral records were defined by assigning annual $\delta^{18}O$ maxima to mid-October, the month of the climatological minimum in SSTs in the southern Mentawai Islands. The annual minimum in SST has a standard deviation of ±1.5 months in instrumental data. Coral X-ray images and annual cycles in coral $\delta^{13}C$ were also used to guide the assignment of annual markers in cases where the $\delta^{18}O$ tie points were ambiguous. Chronologies were interpolated linearly to the coral isotope data, before being resampled to monthly average resolution. Resampling was carried out using a nearest-neighbour (stepwise) interpolation of the geochemical data to approximately daily resolution, before binning data into monthly averages. This step ensures that the correct proportion of each data point was assigned to the monthly bins without causing signal dampening associated with simple linear interpolation. Geochemistry-based internal chronologies for *Porites* coral records have been estimated in previous studies to have an accumulated uncertainty of ±1–3 years per century[57].

High-precision U–Th dates of the fossil corals (Supplementary Table 2)[58,59] use an initial $^{230}Th/^{232}Th$ atomic ratio of $5.7 (\pm 3.1) \times 10^{-6}$ ($2\sigma$). This isochron-inferred value is based on the analysis of 11 coral specimens covering the South Pagai and North Pagai study areas[60]. This initial $^{230}Th/^{232}Th$ value is slightly more constrained than the value of $6.5 (\pm 6.5) \times 10^{-6}$ used in microatoll studies across the broader Mentawai Island chain[61], but more conservative than the high-precision value of $4.4 (\pm 2.2) \times 10^{-6}$ used in other coral palaeoclimate studies that assume secular equilibrium with the bulk Earth $^{232}Th/^{238}U$ value of 3.8 (for example, ref. [28]).

Absolute age assignments for the coral chronologies were determined using a combination of high-precision U–Th dates, alignment with documented tectonic activity in the southern Mentawai Islands[53,61], assignment of distinct $\delta^{13}C$ excursions to large tropical volcanic eruptions[24,62,63], and splicing of coral isotopic records that overlap in time[21] (Supplementary Figs. 12–16). Splicing of overlapping coral sections used the best alignment of interannual variability, working within the constraints provided by all U–Th dates. Coral $\delta^{18}O$ anomalies (after removal of variability at timescales longer than 7 years; see Methods section 'Record filtering') were averaged together across overlapping coral sections to produce the spliced $\delta^{18}O$ anomaly sequences, and details of $\delta^{18}O$ correlations and variance ratios of overlapping sections are given in Supplementary Figs. 14–16.

### IOD reconstruction sequences

The IOD reconstruction covers 500 years since 1240. Detailed descriptions of each section of the reconstruction are provided below:

**1846–2019.** Living modern coral TT01-A-1b from Tinopo was drilled in July 2001 (Supplementary Figs. 2, 12). The $\delta^{18}O$ record from this coral has been previously used to demonstrate that the southern Mentawai Islands represent an optimum site for reconstructing IOD events[18], and the record is extended in this study back to 1936. A previously published[11] short modern coral record from the Saomang site demonstrates the consistency of coral $\delta^{18}O$ records between the Tinopo site on the eastern side of the southern Mentawai Islands and the fossil coral locations on the western side of the southern Mentawai Islands (Extended Data Fig. 1; Supplementary Fig. 12).

The modern-day IOD sequence also uses the coral DMI reconstruction[5] that extends back to 1846, and the instrumental DMI[51,64,65] to continue the IOD record to 2019. Instrumental SST products are not used before 1958 owing to uncertainties in their quality for earlier times[1,66]. Figure 1c, d shows these overlapping records of IOD variability since 1958.

**1770–1820.** Microatoll SI94-A-6 from Siruamata (Supplementary Figs. 3, 13) was originally sampled for earthquake studies along the Mentawai

Island chain and displays a 'hat-shaped' morphology caused by more than 70 cm of uplift during the 1797 earthquake[53–55,67]. The coral slab was later analysed to examine $\delta^{13}C$ signals related to vertical uplift[62]. The coral $\delta^{13}C$ record shows a clear shift associated with the 1797 earthquake and uplift event at this site, along with a distinct year with no seasonal $\delta^{13}C$ peak that is associated with the 1815 Tambora eruption. In reef environments that are well flushed by open ocean water it has been demonstrated that *Porites* microatoll $\delta^{18}O$ produces a reliable record of climate variability that is comparable to records generated from upward growing *Porites* corals[68].

The originally defined internal chronology of the SI94-A-6 isotope record[62] is inconsistent with regional climatology. It has $\delta^{18}O$ maxima falling on average in July, rather than coinciding with the annual SST minima in October, and produces positive IOD anomalies that have a physically implausible timing that is inconsistent with the seasonal phase-locking of IOD activity[3,48]. To address this, we constructed a chronology for the coral isotope record that is consistent with the methodology used for all of the other southern Mentawai Island corals, while still honouring the unambiguous fixed-time markers provided by the coral $\delta^{13}C$ responses to the 1797 earthquake and the 1815 eruption.

The revised chronology results in extreme negative $\delta^{18}O$ anomalies in 1790–91, and more intensely in 1791–92, which are characteristic of the basin-wide warming that accompanies El Niño events[8]. These anomalies correspond with the great El Niño of 1790–94 (refs. [25,69]), thought to be among the most severe in the written record[69]. A positive IOD event recorded in this coral in 1792 probably contributed to the regional impacts of the 1790–94 severe El Niño sequence[69], including historical records of famine in Madras, India, that killed up to half of the population there in 1792. A positive IOD event in 1783 also coincides with historical accounts[69] of famine throughout India and a protracted El Niño event from 1782–84.

**1641–99.** This sequence is comprised of two overlapping coral records: SMG01-A-10c from Soamang and NP01-A-3 from Silabu (Supplementary Figs. 4, 5, 14). Since these corals come from two different sites approximately 50 km apart, they are not expected to record consistent $\delta^{13}C$ responses to tectonic activity, which varies considerably over such length scales in the southern Mentawai Islands[61]. The chronology of this sequence is constrained by four U–Th ages, two from each coral. Within the constraints of the U–Th ages, the interannual patterns of coral $\delta^{18}O$ allow the internal chronology of the two coral records to be confidently spliced over a 7-year interval of overlap.

The assigned calendar ages for this sequence were aligned to historical climate information and the microatoll-based earthquake history from the region. It is assumed that the end of the sequence (and death of the coral colony) corresponds to the large earthquake and uplift event[61] focused on the North and South Pagai islands in 1703 (±10 years), allowing for erosion since this time of the last years of coral growth in SMG01-A-10c. Extreme positive IOD events in the coral sequence coincide with historical evidence[27] of intense drought and famine in Indonesia in 1660 and 1675. A strong negative $\delta^{18}O$ anomaly following the 1660 extreme positive IOD event coincides with historical evidence for a very strong El Niño event in this year (that is, a positive IOD followed by basin-wide warming in the Indian Ocean related to a co-occurring El Niño event)[25,26]. The calendar age assignments of the spliced sequence could be up to 8 years younger or older than those given here based on alignment to tectonic and historical information, while still staying within the $\pm 2\sigma$ bounds of all four U–Th ages.

A partial growth unconformity in coral NP01-A-3 occurred during 1651, but there is no evidence (from transect E where growth was continuous) that this was caused by a climatic event. Conversely, there is no evidence of coral growth disruption during the extreme 1675 positive IOD event (transect A), although a negative anomaly in coral $\delta^{13}C$ during the 1675 event may be an indicator of a relative increase of heterotrophy of the coral (relative to photosynthesis of zooxanthellae), or of surface ocean $^{13}C$ depletion from ocean upwelling. Extreme positive IOD events of equivalent size are known from the mid-Holocene and also occurred without disruption to coral growth[11].

**1452–1601.** This sequence is comprised of two overlapping coral cores, P01-C-2a and P01-C-2b, collected from a single coral colony at Pororogat (Supplementary Figs. 6, 15). The fossil coral colony has a 'cup-shaped' morphology, indicative of growth in a subsiding setting[53,55,61,70]. Core P01-C-2b was collected from the lower central core of the colony, representing the older part of coral growth. Core P01-C-2a was drilled through the raised outer rim, capturing the younger section of colony growth. The two cores can be aligned using distinctive growth bands (Supplementary Fig. 6). The geochemical analysis also provides 15 years of overlap where the $\delta^{18}O$ and $\delta^{13}C$ records can be spliced together with very high confidence.

Two precise U–Th ages from near the base of the P01-C-2b core together constrain the absolute age of the start of this coral sequence to within ±10 years. Within the same section a clear $\delta^{13}C$ excursion occurs, analogous to the SI94-A-6 coral response to the Tambora eruption. We ascribe this to the Kuwae eruption; the second-largest eruption of the last millennium[24], which is known to have caused far-reaching ash deposits and climate responses. The absolute age of the Kuwae eruption is debated. The year of eruption has long been ascribed to 1452, but was recently revised to 1458 using ice-core chronologies[24,71]. Re-evaluation of tree-ring chronologies maintain 1452 as the Kuwae eruption year[72]. The two U–Th ages are most consistent with an eruption in 1452, but could still accommodate a 1458 eruption year within the $\pm 2\sigma$ bounds of the two U–Th ages. We note, however, that an eruption year of 1458 cannot be accommodated if the coral U–Th ages are calculated using the less conservative initial $^{232}Th/^{230}Th$ atomic ratio of $4.4\ (\pm 2.2) \times 10^{-6}$. Consideration of the other U–Th age constraints on the coral sequence is also more consistent with a 1452 eruption year (Supplementary Fig. 15), and so, on the balance of evidence, we assign the volcanic $\delta^{13}C$ excursion to 1452. The calendar age assignments of the spliced sequence could be up to 4 years younger or 14 years older than those given here, based on alignment to the 1452 Kuwae eruption event, while still staying within the $\pm 2\sigma$ bounds of all five U–Th ages.

The internal chronology of this coral sequence represents 150 years of coral growth, and is aided by strong seasonal $\delta^{13}C$ cycles, particularly in the first ~80 years of coral growth. A 4.5-year gap (constrained by geochemical data and X-ray images) in the P01-C-2b isotope record is associated with a section of calcite diagenesis where the geochemical signals are not reliable for climate analysis. Based on the assignment of the volcanic $\delta^{13}C$ marker at the start of the chronology to 1452, and an estimated uncertainty on the internal chronology of up to ±3 years per century[57], the uppermost year of the coral sequence is 1601 ± 5 years. The X-rays indicate at least two further years of coral growth that has been eroded from the uppermost surface of the fossil coral colony. Within the uncertainty of the upper age of this coral sequence, and of previous microatoll studies[53,61], the death of this coral could be related to earthquakes in 1597 or 1613 (±10 years)[61]. We consider that the link to the ~1613 earthquake event is most probable because (1) the coral core indicates substantial surface erosion, (2) microatolls from nearby (Bulasat) experienced strong (more than 50 cm) uplift during the ~1613 event, and (3) tectonic uplift in 1597 appears to have been negligible at Bulasat (5 ± 3 cm) and was instead focused on more northerly locations in the Mentawai island chain[61]. A sudden drop in coral $\delta^{13}C$ in 1586 of our coral sequence may instead be indicative of a small subsidence event at Pororogat during the culmination of this earthquake super-cycle. This $\delta^{13}C$ signal occurred approximately 17 years before the death of this coral, and is very similar to the 16-year separation of the 1597 and 1613 (±10 years) earthquakes identified in coral microatoll growth[61].

The absolute chronology of the upper section of this coral sequence is consistent with historical evidence of climate disturbance across tropical Asia. Beginning around 1590, the coral data document a rapid

increase in mean $\delta^{18}O$ isotope levels and frequent positive IOD events (in about 1592, 1594, 1597 and 1600). This marked increase in positive IOD activity after 1590 coincides with the beginning of the 'seventeenth century crisis' in tropical Asia, in which droughts, famines and deaths were widespread, and which resulted in large-scale economic and political disruption[26].

**1240–1305.** This sequence is comprised of three overlapping coral records from the Saomang site: SMG01-A-2, SMG01-A-4a and SMG01-A-5b (Supplementary Figs. 7–9, 16). The anchor coral for this chronology is SMG01-A-4a, constrained by a U–Th date of 1253 (±9 years). The location of this U–Th date coincides with a $\delta^{13}C$ event where no summer $\delta^{13}C$ peak is recorded, making that year distinct relative to surrounding mean $\delta^{13}C$ cycles in this coral. The magnitude of mean annual cycles in the Saomang corals are smaller than for the coral sequences containing the Tambora and Kuwae eruption signals, and hence the absolute magnitude of the possible volcanic signal is not as large in coral $\delta^{13}C$. We ascribe this $\delta^{13}C$ event to the 1257 eruption of Samalas; the largest volcanic eruption of the last millennium[24,73,74]. This provides a reasonably firm absolute chronology for the SMG01-A-4a coral, which extends from 1255 to 1269. Within the constraints of the U–Th date, this sequence could be up to 2 years younger or 16 years older than the absolute chronology that is aligned to the Samalas eruption date.

Unconformities and off-axis growth prevented further extension of this sequence using the SMG01-A-4a coral colony, but two additional corals allow extension of the sequence. The older end of the sequence comes from coral SMG01-A-2. A U–Th date for this coral provides only a limited (±62 years) constraint on the absolute age of this coral owing to high detrital $^{232}Th$ content. However, within this age constraint an overlap of 5 years with the SMG01-A-4a coral provides a good alignment of the $\delta^{18}O$ and $\delta^{13}C$ records from these cores, and places the lower date of the sequence at 1240. No other viable splicing scenarios are found within this sequence and so we assume the splice to be robust but cannot rule out the possibility that the absolute age of the SMG01-A-2 coral could be older by 6 to 27 years than ascribed here through splicing of the record to the well-dated SMG01-A-4a coral (that is, within the U–Th dating constraints but not overlapping with the other corals in this sequence).

The younger end of this coral sequence comes from coral SMG01-A-5b, which is constrained by two U–Th dates that also have large uncertainties (±40 years and ±46 years) due to high detrital $^{232}Th$ content. Four years of overlap with the SMG01-A-4a coral provides a good alignment of the $\delta^{18}O$ and $\delta^{13}C$ records from these cores, including overlap through a positive IOD event in 1267. This alignment places the upper end of this sequence at around 1305. Within the age uncertainty of the U–Th dates from the SMG01-A-5b coral we cannot rule out that this coral could be younger by between 5 and 52 years than ascribed here through splicing of the record to the well dated SMG01-A-4a coral (that is, within the U–Th dating constraints but not overlapping with the other corals in this sequence). There is limited tectonic and historical information to draw upon to help us further constrain the age of the coral sequence. However, the South Pagai region is thought to have experienced a sudden, large subsidence event around 1314 and a large uplift event in 1350[53,61,75]. We see no evidence for abrupt offsets in coral $\delta^{13}C$ in the SMG01-A-5b record that could be tied to these tectonic events, giving confidence that the coral is not more than 10 years younger than the absolute age derived from splicing to the SMG01-A-4a coral record. The finding of reduced IOD variability before 1590 would remain robust even if the thirteenth-century corals were not part of a time-overlapping sequence.

### Record filtering

Interannual IOD variability was isolated in the coral records by removing variability at timescales longer than 7 years to produce $\delta^{18}O$ anomaly records (Supplementary Figs. 12–16). Removing variability at timescales longer than 7 years replicates methods associated with calculation of the DMI[1], and will remove any long-term environmental or tectonic trends from the coral $\delta^{18}O$ datasets. To minimize the effects of spurious, method-dependent filtering at the start and end of the coral records, variability at timescales longer than 7 years was removed from the coral $\delta^{18}O$ records by subtracting the average of three filtering methods; namely, a 7-year 5th-order Butterworth lowpass filter, a 7-year LOESS filter (weighted 2nd-order polynomial regression), and a 7-year LOWESS filter (weighted linear regression).

### Reference interval

All analyses are carried out relative to the 1961–1990 interval. This is a standard 30-year climatology reference, and the 1961–1990 interval is selected because it is covered in full by coral, instrumental and model data, and in the coral/instrumental data avoids the two extreme positive IOD events in 1994 and 1997 that are unusual in the context of the twentieth century and may create bias if included in the reference interval. The reference interval does, however, include the extreme positive IOD event in 1961.

### IOD event detection

Positive IOD event occurrence was assessed by first smoothing the monthly-resolved coral $\delta^{18}O$ anomaly data with a 3-month moving average. Positive IOD events were detected when the 3-month average exceeded a threshold of $+1.5\sigma$ (based on variability of the modern coral between 1961–1990) for at least one month during the July–December IOD season. If a threshold of $+3\sigma$ was also exceeded during the July–December interval then an extreme positive IOD event was classified.

The same event detection method was applied to the DMI datasets. The coral DMI[5] and instrumental DMIs were filtered in the same way as for the coral $\delta^{18}O$ records to remove variability at timescales longer than 7 years. All records were referenced relative to their 1961–1990 climatology, with the OISSTv2 DMI dataset scaled to match the standard deviation of the ERSSTv5 DMI over their common interval since November 1981. In our assessments of IOD variability we use the instrumental DMI derived from OISSTv2[51] from 1982–2019, and from ERSSTv5[64] and HadISST[65] from 1958–1982. The positive IOD event detection method reliably identifies known positive IOD events[18] (Fig. 1).

In this study we examine only positive IOD events, which have a clear and unambiguous signal at our study site[18]. Negative IOD events are less well characterized and tend to be weaker than positive events[3,76]. In particular, it remains to be tested whether these events can be adequately described using data from just the eastern Indian Ocean sector, given that the positive SST anomalies related to a negative IOD event may be difficult to differentiate from the basin-wide warming associated with El Niño events in this area.

### IOD event analysis

The magnitude of extreme positive IOD events was assessed relative to the 1997 event; the strongest event to have occurred in the observational record. This comparison was made for the peak magnitude of monthly mean $\delta^{18}O$ anomalies during the extreme positive event, and for the integrated July–December average of $\delta^{18}O$ anomalies across each event. The comparison of the 1997 and stronger 1675 events includes uncertainty estimates, based on the standard error of the mean across replicate measurements of the individual $\delta^{18}O$ samples that comprise the peak monthly $\delta^{18}O$ anomaly for these events (Extended Data Fig. 6a, b). The standard error calculation reflects 11 replicate analyses across the 5 samples that contribute to the peak monthly mean value for the 1997 event, and for the 1675 event reflects 11 replicate analyses across the 4 samples that contribute to the peak monthly mean value.

### IOD and ENSO variability

Variability of the IOD through the last millennium (Fig. 3) was examined by calculating July–December IOD season averages of coral $\delta^{18}O$ and

DMI anomaly data (after filtering to remove variability at timescales longer than 7 years). The standard deviation was calculated for 30-year windows, stepped by 5 years, and expressed as a percentage difference relative to variability in the 1961–1990 reference interval.

We restrict our analysis of interannual ENSO variability to an analogous coral-based dataset for the last millennium from the central Pacific (Dee, S. G. et al., manuscript in preparation and refs. [21,28,29]). This allows for consistent data analysis methods, compares equivalent ocean-based signals directly from the NINO3.4 and eastern DMI regions, and avoids assumptions of atmospheric teleconnection stability which may affect the reliability of other available interannual ENSO reconstructions[32]. The coral-based ENSO datasets were detrended to isolate interannual ENSO variability using a 2–7 year bandpass filter. The standard deviation was calculated for July–June annual averages across 30-year windows, stepped by 5 years. The fossil corals from Palmyra are referenced to 1961–1990 data from the modern Palmyra coral, and the fossil coral from Christmas Island is referenced to 1961–1990 data from the modern Christmas Island coral. Calculation of moving 30-year standard deviations replicates the analysis previously used to examine coral-based data of ENSO variance changes[28], noting that a 1968–1998 reference interval was used in that study. IOD and ENSO variability calculated as moving 30-year standard deviations are less susceptible to method-related variations caused by threshold choices of event detection approaches.

Comparison of the instrumental DMI and modern coral data with indices of ENSO variability (including indices for differentiating central Pacific and eastern Pacific type ENSO variability)[33,77] is shown in Supplementary Fig. 17 and Supplementary Table 3.

### CESM1-LME analysis

IOD event occurrence and variability in the CESM1-LME simulations (850–2005; http://www.cesm.ucar.edu/projects/community-projects/LME/)[41] was primarily examined using the 13 full-forcing simulations. We note that atmospheric fields are not available for the first ensemble member of the CESM1-LME full-forcing experiments for the years 850–1699. We used SST fields to construct the model DMI, and the model DMI was filtered to remove variability at timescales longer than 7 years using the same methods applied to the coral reconstruction and instrumental DMI data. IOD events were also detected in the model DMI using the same methodology. Comparisons with tropical Pacific variability in the CESM1-LME use the NINO3.4 index from the climate diagnostics package (available for full-forcing ensemble members 1–10), and calculation of the Tripole Index of the Interdecadal Pacific Oscillation from SST fields[45].

The performance of the model compared with observational and reconstructed data for IOD variability was assessed (Extended Data Figs. 2, 3, 8; Supplementary Fig. 18), and the mechanisms associated with intervals of low and high IOD variability, and with decades of rare and frequent positive IOD events, were examined (Fig. 4; Extended Data Figs 9, 10). The CESM1-LME simulations reproduce the coupling of Indo-Pacific climate variability (Fig. 4), though may underestimate the magnitude inferred by palaeoclimate reconstructions (Fig. 3).

The large ensemble allows for testing of forced and unforced (internal) variability (Supplementary Figs. 19–22). We find no evidence in the CESM1-LME simulations for external forcing of the mid-millennium shift in IOD–ENSO variability or for the unusually high IOD–ENSO variability of the seventeenth century, suggesting that these changes may be within the large range of changes in tropical climate variability that can occur due to unforced internal variability[15,16,21,28]. Pseudoproxy tests[19] using the CESM1-LME further suggest that the magnitudes of reconstructed changes in IOD variability during the last millennium, relative to variability in the 1961–1990 interval, are larger than expected from forced and unforced variability of the CESM1-LME model. We note that regression errors used in this pseudoproxy test[19] may be underestimated owing to sparse information on the coral $\delta^{18}O$–salinity relationship[78].

### IOD recurrence risk

IOD event recurrence (Extended Data Fig. 8) was calculated as the number of years between adjacent positive IOD events. Event times between the end and start of adjacent sequences (that is, where there are gaps in the last millennium reconstruction) were omitted. The probability (with 95% confidence bounds) of subsequent positive IOD events across the last millennium coral reconstruction was assessed using an empirical Kaplan–Meier cumulative distribution function through the MATLAB 'ecdf' function (Extended Data Fig. 8c).

### Significance testing

The significance reported for all linear correlations takes into account autocorrelation of the coral, instrumental and model datasets through calculation of an effective sample size ($n_{eff}$) based on the lag(1) autocorrelation. The significance of differences in distributions of climate parameters is assessed using the Kolmogorov–Smirnov test.

## Data availability

The coral $\delta^{18}O$ data needed to reproduce the results are available at the World Data Service for Paleoclimatology at http://www.ncdc.noaa.gov/paleo/study/28451. Archived data includes coral $\delta^{18}O$ and $\delta^{18}O$ anomaly data, U-Th age data, reconstructed positive IOD event years, and the moving 30-year standard deviation of July–December IOD variability.


51. Reynolds, R. W., Rayner, N. A., Smith, T. M., Stokes, D. C. & Wang, W. An improved in situ and satellite SST analysis for climate. *J. Clim*. **15**, 1609–1625 (2002).
52. Adler, R. et al. The Global Precipitation Climatology Project (GPCP) monthly analysis (new version 2.3) and a review of 2017 global precipitation. *Atmosphere* **9**, 138 (2018).
53. Sieh, K. et al. Earthquake supercycles inferred from sea-level changes recorded in the corals of west Sumatra. *Science* **322**, 1674–1678 (2008).
54. Natawidjaja, D. H. et al. Source parameters of the great Sumatran megathrust earthquakes of 1797 and 1833 inferred from coral microatolls. *J. Geophys. Res. Solid Earth* **111**, B06403 (2006).
55. Zachariasen, J., Sieh, K., Taylor, F. W., Edwards, R. L. & Hantoro, W. S. Submergence and uplift associated with the giant 1833 Sumatran subduction earthquake: evidence from coral microatolls. *J. Geophys. Res. Solid Earth* **104**, 895–919 (1999).
56. McGregor, H. V. & Abram, N. J. Images of diagenetic textures in *Porites* corals from Papua New Guinea and Indonesia. *Geochem. Geophys. Geosyst.* **9**, Q10013 (2008).
57. DeLong, K. L., Quinn, T. M., Taylor, F. W., Shen, C.-C. & Lin, K. Improving coral-base paleoclimate reconstructions by replicating 350 years of coral Sr/Ca variations. *Palaeogeogr. Palaeoclimatol. Palaeoecol.* **373**, 6–24 (2013).
58. Shen, C.-C. et al. High-precision and high-resolution carbonate $^{230}$Th dating by MC-ICP-MS with SEM protocols. *Geochim. Cosmochim. Acta* **99**, 71–86 (2012).
59. Cheng, H. et al. Improvements in $^{230}$Th dating, $^{230}$Th and $^{234}$U half-life values, and U–Th isotopic measurements by multi-collector inductively coupled plasma mass spectrometry. *Earth Planet. Sci. Lett.* **371–372**, 82–91 (2013).
60. Shen, C.-C. et al. Variation of initial $^{230}$Th/$^{232}$Th and limits of high precision U–Th dating of shallow-water corals. *Geochim. Cosmochim. Acta* **72**, 4201–4223 (2008).
61. Philibosian, B. et al. Earthquake supercycles on the Mentawai segment of the Sunda megathrust in the seventeenth century and earlier. *J. Geophys. Res. Solid Earth* **122**, 642–676 (2017).
62. Gagan, M. K. et al. Coral $^{13}$C/$^{12}$C records of vertical seafloor displacement during megathrust earthquakes west of Sumatra. *Earth Planet. Sci. Lett.* **432**, 461–471 (2015).
63. Gao, C., Robock, A. & Ammann, C. Volcanic forcing of climate over the past 1500 years: an improved ice core-based index for climate models. *J. Geophys. Res.* **113**, D23111 (2008).
64. Smith, T. M., Reynolds, R. W., Peterson, T. C. & Lawrimore, J. Improvements to NOAA's historical merged land-ocean surface temperature analysis (1880-2006). *J. Clim*. **21**, 2283–2296 (2008).
65. Rayner, N. A. et al. Global analyses of sea surface temperature, sea ice, and night marine air temperature since the late nineteenth century. *J. Geophys. Res*. **108**, 4407 (2003).
66. Chan, D., Kent, E. C., Berry, D. I. & Huybers, P. Correcting datasets leads to more homogeneous early-twentieth-century sea surface warming. *Nature* **571**, 393–397 (2019).
67. Philibosian, B. et al. Rupture and variable coupling behavior of the Mentawai segment of the Sunda megathrust during the supercycle culmination of 1797 to 1833. *J. Geophys. Res. Solid Earth* **119**, 7258–7287 (2014).
68. McGregor, H. V., Fischer, M. J., Gagan, M. K., Fink, D. & Woodroffe, C. D. Environmental control of the oxygen isotope composition of *Porites* coral microatolls. *Geochim. Cosmochim. Acta* **75**, 3930–3944 (2011).
69. Grove, R. & Adamson, G. in *El Niño in World History* (eds Richard Grove & George Adamson) 81–92 (Palgrave Macmillan, 2018).
70. Natawidjaja, D. H. et al. Paleogeodetic records of seismic and aseismic subduction from central Sumatran microatolls, Indonesia. *J. Geophys. Res. Solid Earth* **109**, B04306 (2004).

71. Plummer, C. T. et al. An independently dated 2000-yr volcanic record from Law Dome, East Antarctica, including a new perspective on the dating of the 1450s CE eruption of Kuwae, Vanuatu. *Clim. Past* **8**, 1929–1940 (2012).
72. Esper, J., Büntgen, U., Hartl-Meier, C., Oppenheimer, C. & Schneider, L. Northern Hemisphere temperature anomalies during the 1450s period of ambiguous volcanic forcing. *Bull. Volcanol.* **79**, 41 (2017).
73. Guillet, S. et al. Climate response to the Samalas volcanic eruption in 1257 revealed by proxy records. *Nat. Geosci.* **10**, 123–128 (2017).
74. Lavigne, F. et al. Source of the great A.D. 1257 mystery eruption unveiled, Samalas volcano, Rinjani Volcanic Complex, Indonesia. *Proc. Natl Acad. Sci. USA* **110**, 16742–16747 (2013).
75. Philibosian, B. et al. An ancient shallow slip event on the Mentawai segment of the Sunda megathrust, Sumatra. *J. Geophys. Res. Solid Earth* **117**, (2012).
76. Lim, E.-P. & Hendon, H. H. Causes and predictability of the negative Indian Ocean Dipole and its impact on La Niña during 2016. *Sci. Rep.* **7**, 12619 (2017).
77. Ren, H.-L. & Jin, F.-F. Niño indices for two types of ENSO. *Geophys. Res. Lett.* **38**, L04704 (2011).
78. Conroy, J. L. et al. Spatiotemporal variability in the $\delta^{18}O$-salinity relationship of seawater across the tropical Pacific Ocean. *Paleoceanography* **32**, 484–497 (2017).

**Acknowledgements** This research was supported by an Australian Research Council QEII Fellowship to N.J.A. (DP110101161; including C.-C.S., H.C. and R.L.E.) and the ARC Centre of Excellence for Climate Extremes (CLEX; CE170100023; to N.J.A., N.M.W., M.H.E. and C.C.U.). Further support to N.J.A. was provided by ARC Discovery Project DP140102059 and Future Fellowship FT160100029. B.E. was supported by an Australian Research Training Program scholarship and B.C.D. received scholarship support from the ARC Centre of Excellence for Climate System Science (CE110001028). M.H.E. is also supported by the Earth Science and Climate Change Hub of the Australian Government's National Environmental Science Programme (NESP). C.C.U. acknowledges support by the US National Science Foundation (AGS-1602455). C.-C.S. thanks the Science Vanguard Research Program of the Ministry of Science and Technology (108-2119-M-002-012) and the Higher Education Sprout Project of the Ministry of Education, Taiwan, Republic of China (108L901001) for support. H.C. acknowledges support by the National Natural Science Foundation of China (NSFC 41888101). We gratefully acknowledge the Ministry of Research, Technology and Higher Education, and the Director of Intellectual Property Management as Secretary of the Coordinating Team for Foreign Research Permit (TKPIPA) for the research permit in Indonesia. Fieldwork was carried out in 2001 under research permit 2889/II/KS/2001, supported by W. Hantoro and the Indonesian Institute of Sciences. We thank W. Hantoro, B. Suwargadi, D. Prayudi, I. Suprianto, M. Gagan, K. Glenn, T. Watanabe, H. Scott-Gagan, and K. Sieh for assistance with fieldwork, J. Cowley, J. Cali, D. Becker, A. Kimbrough, S. Wong, B. Plunkett, S. Sosdian, H. Scott-Gagan and C.-H. Hsu for laboratory support, the NCAR CESM1 modelling group for making their last millennium ensemble simulations available, and Australia's National Computational Infrastructure and CLEX Computational Modeling Systems team for data hosting and support. We acknowledge Python Software Foundation (Python version 3.7.2), MathWorks Inc. (MATLAB Release 2014a) and R. Pawlowicz (M_Map mapping package for MATLAB, version 1.4g) for software used in analysis and figure generation. Any use of trade, firm or product names is for descriptive purposes only and does not imply endorsement by the US Government. We thank J. Addison and R. Halley (US Geological Survey) for internal reviews of this manuscript before submission, and S. Eggins for leadership and guidance.

**Author contributions** N.J.A. designed the study and led the analysis, interpretation and writing. B.E., B.C.D. and J.B.W. contributed to coral sample milling and geochemical analysis. N.J.A. and N.M.W. led the model analysis with assistance from M.H.E. and C.C.U. B.P. aided in chronology development for the fossil coral records, S.Y.C. provided coral palaeoclimate expertise, T.-L.K., C.-C.S., H.C. and R.L.E. carried out U–Th analyses, and D.H. helped with the statistical tests. All authors contributed to discussions during preparation of the manuscript.

**Competing interests** The authors declare no competing interests.

**Additional information**

**Supplementary information** is available for this paper at https://doi.org/10.1038/s41586-020-2084-4.

**Correspondence and requests for materials** should be addressed to N.J.A.

**Peer review information** *Nature* thanks Matthias Prange, Diane M. Thompson and the other, anonymous, reviewer(s) for their contribution to the peer review of this work.

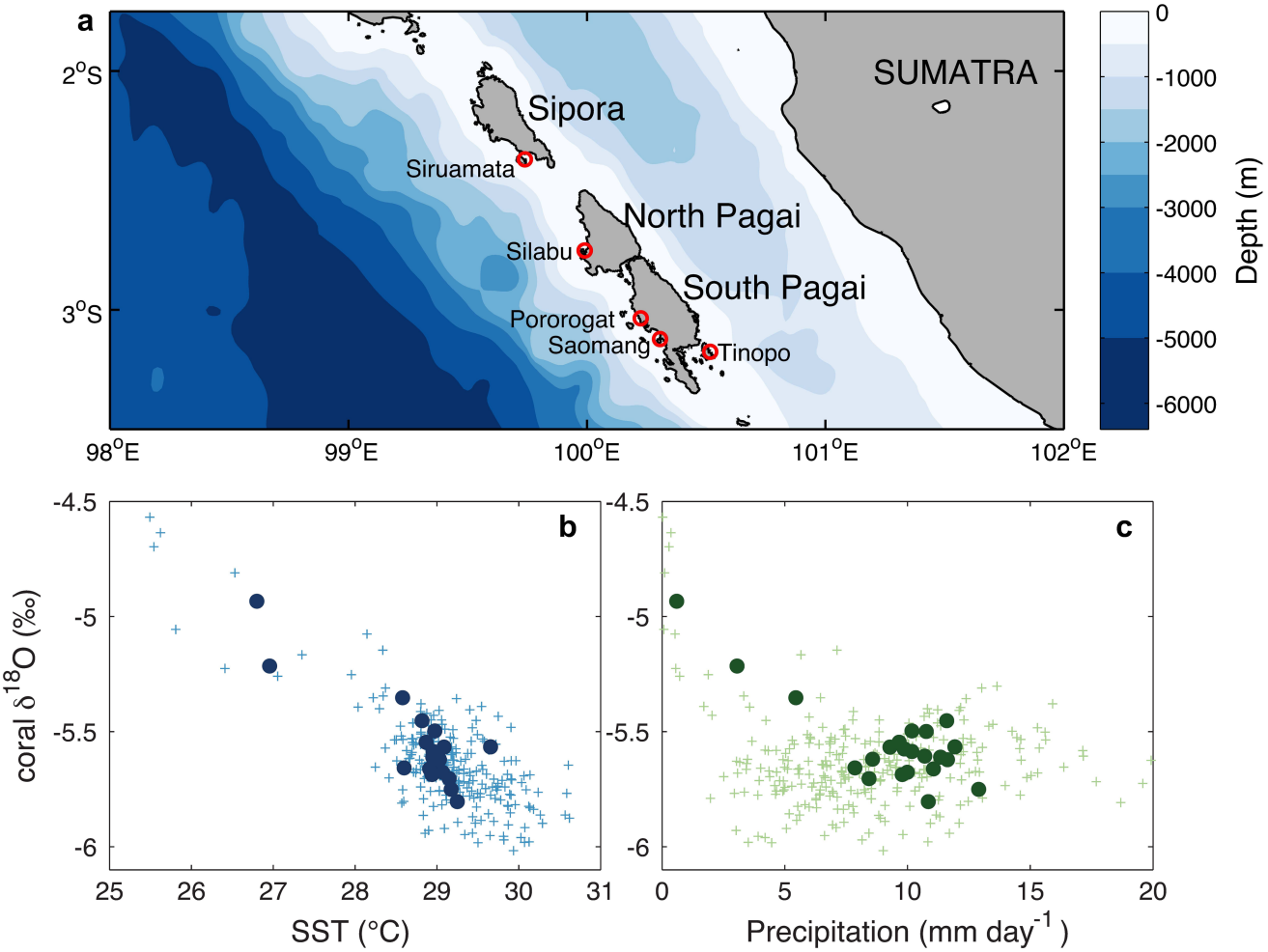


**Extended Data Fig. 1 | Location map and coral $\delta^{18}O$–climate relationships.** **a**, Coral samples used in this study were collected from the southern Mentawai Islands, offshore of Sumatra in the eastern Indian Ocean. Study sites are Tinopo (coral TT01-A-1b), Saomang (corals SMG01-A-2, SMG01-A-4a, SMG01-A-5b and SMG01-A-10c), Pororogat (cores P01-C-2a and 2b), Silabu (coral NP01-A-3) and Siruamata (coral SI94-A-6). **b**, **c**, Relationships between modern coral $\delta^{18}O$ (TT01-A-1b) and instrumental records[51,52] of local SST (**b**) and precipitation (**c**) at 3° S, 100° E. Crosses show monthly average relationship and filled circles show relationship for July–December averages.

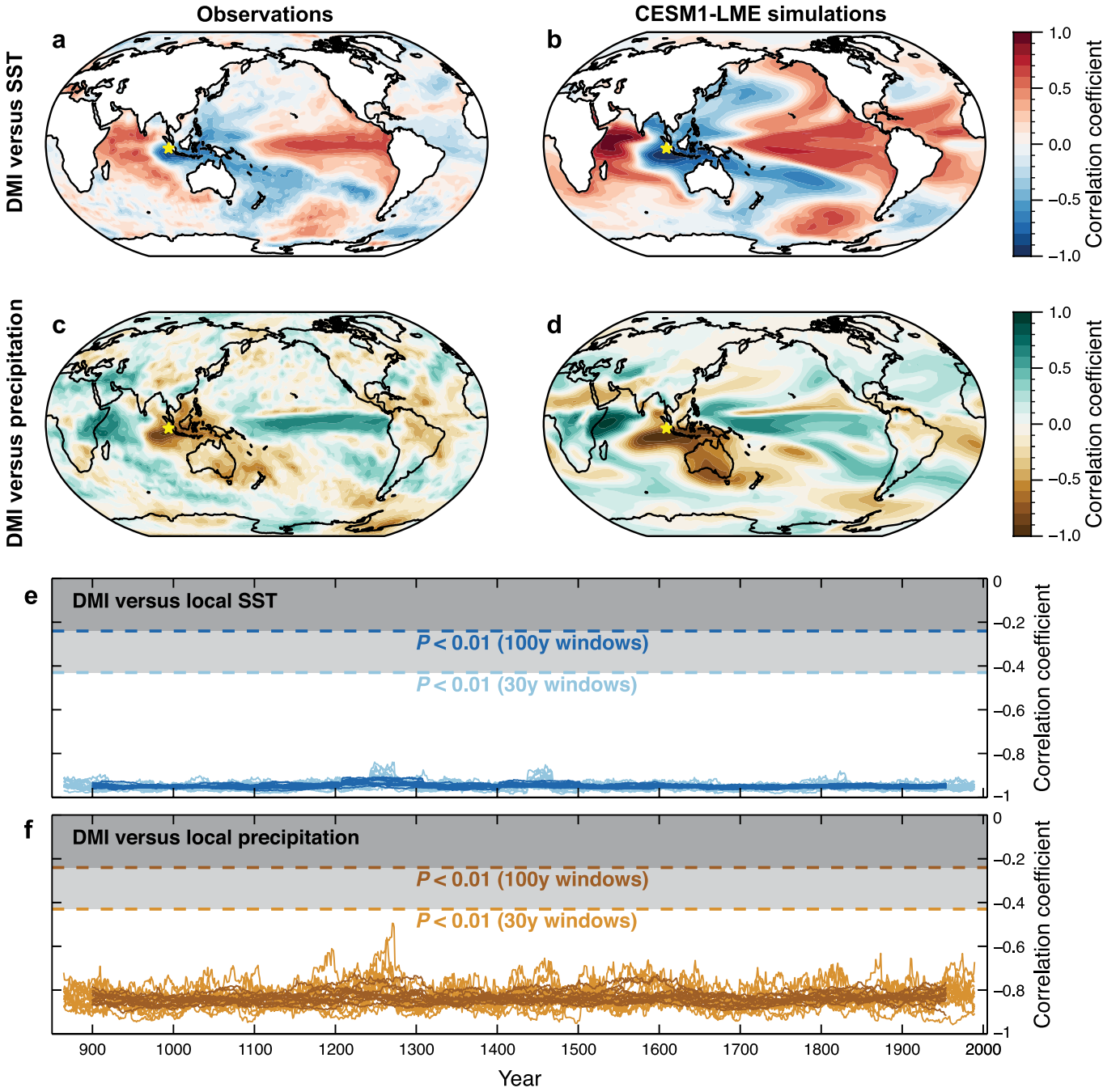


**Extended Data Fig. 2 | Observed and modelled IOD correlations.** **a**–**d**, Correlations of the DMI with SST (upper) and precipitation (lower) in instrumental data (**a**, **c**) and in the CESM1-LME simulations (**b**, **d**). Correlations are for July–December IOD season averages and cover 1982–2018 (**a**), 13 simulations of 850–2005 (15,028 years) (**b**), 1979–2018 (**c**) and 12 simulations of 850–2005 (13,872 years) (**d**). The study area (3° S, 100° E) is marked with yellow stars. **e**, **f**, Moving correlations of local SST (**e**) and precipitation (**f**) with the DMI in the CESM1-LME simulations for 30-year (light) and 100-year (dark) windows, demonstrating a significant ($P < 0.01$) and stable relationship through time of climate anomalies at our study site with the DMI.

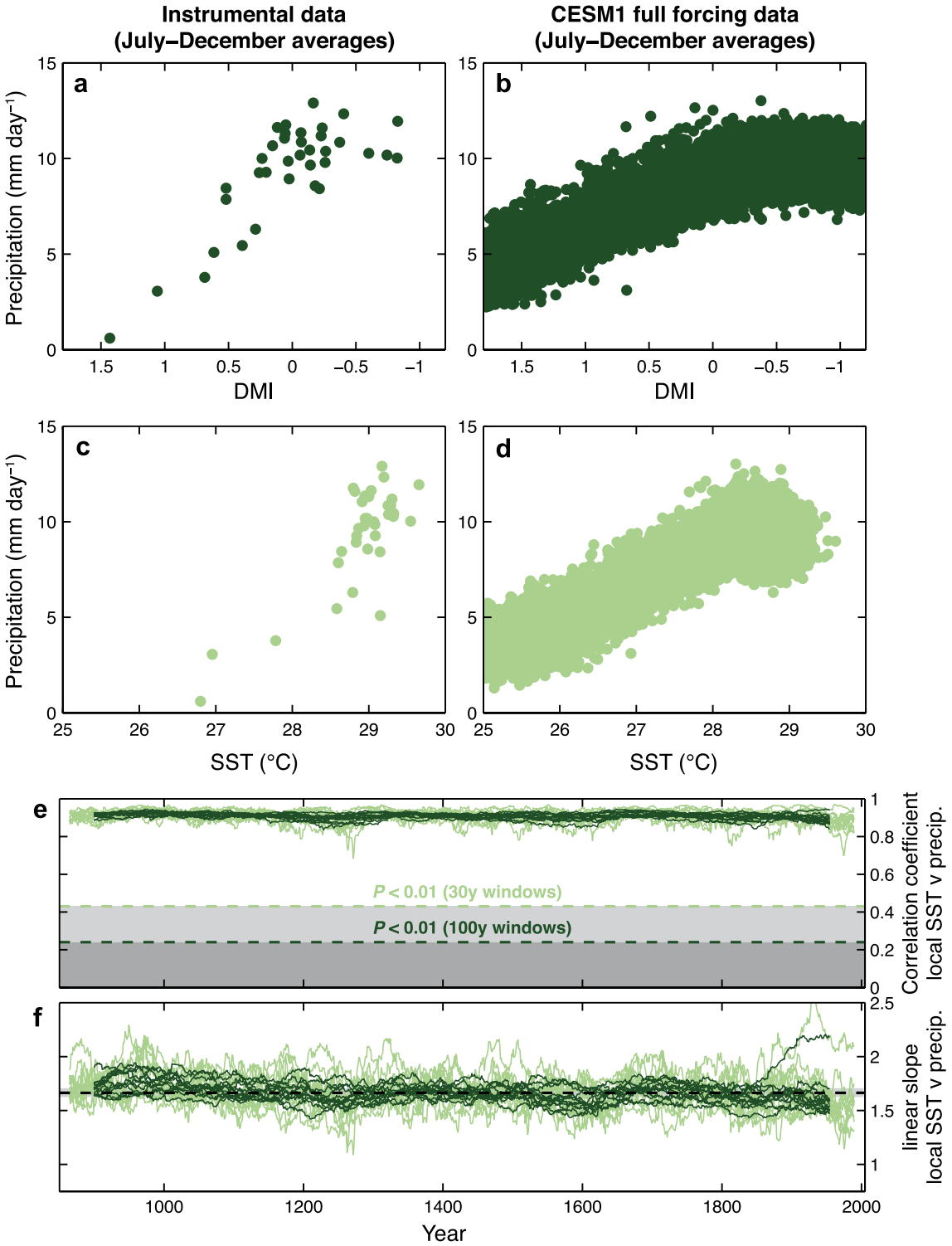


**Extended Data Fig. 3 | Linearity of the response of rainfall in the southern Mentawai Islands to positive IOD events. a–d**, July–December averages of precipitation in the southern Mentawai Islands (3° S, 100° E) are plotted against the DMI (**a**, **b**) and local SST (**c**, **d**). Left-side panels (**a**, **c**) show relationship in instrumental data (1982–2018), and right-side panels (**b**, **d**) show relationship in full-forcing CESM1-LME simulations (12 atmospheric simulations each spanning 850–2005). **e**, **f**, Moving correlation (**e**) and moving slope (**f**) of the linear relationship of local SST with precipitation in the CESM1-LME simulations for 30-year (light) and 100-year (dark) windows. The instrumental and model data demonstrate the strong ($P < 0.01$) and stable linear response of rainfall at the study site to IOD variability, particularly during positive IOD events (positive DMI values and cool SST anomalies).

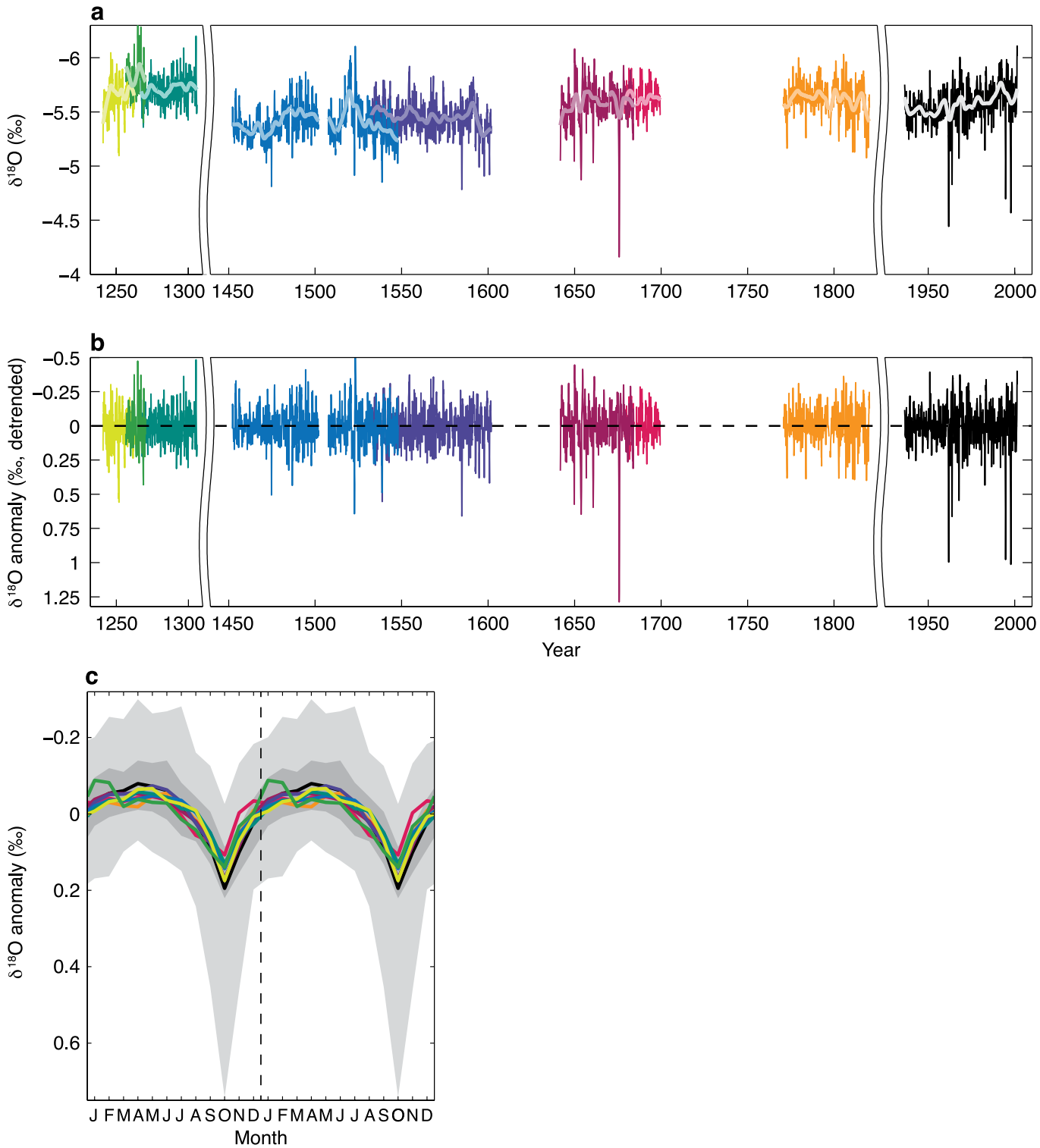


**Extended Data Fig. 4 | Coral data used in this study. a**, Monthly-resolution data (dark) and 7-year filter (light) of the nine coral $\delta^{18}O$ records used in this study. **b**, Monthly $\delta^{18}O$ anomalies after removal of 7-year filter. **c**, Mean annual $\delta^{18}O$ cycle of the modern coral from our study area (black), along with 25–75% (dark shading) and 5–95% (light shading) distributions around the mean. Coloured curves give the mean annual $\delta^{18}O$ cycle of each fossil coral record. Internal chronologies of the coral records were established by assigning the annual $\delta^{18}O$ maxima to October, the coolest month on average in the southern Mentawai Islands (Methods). Details of the coral samples and $\delta^{18}O$ records are provided in the Supplementary Information.

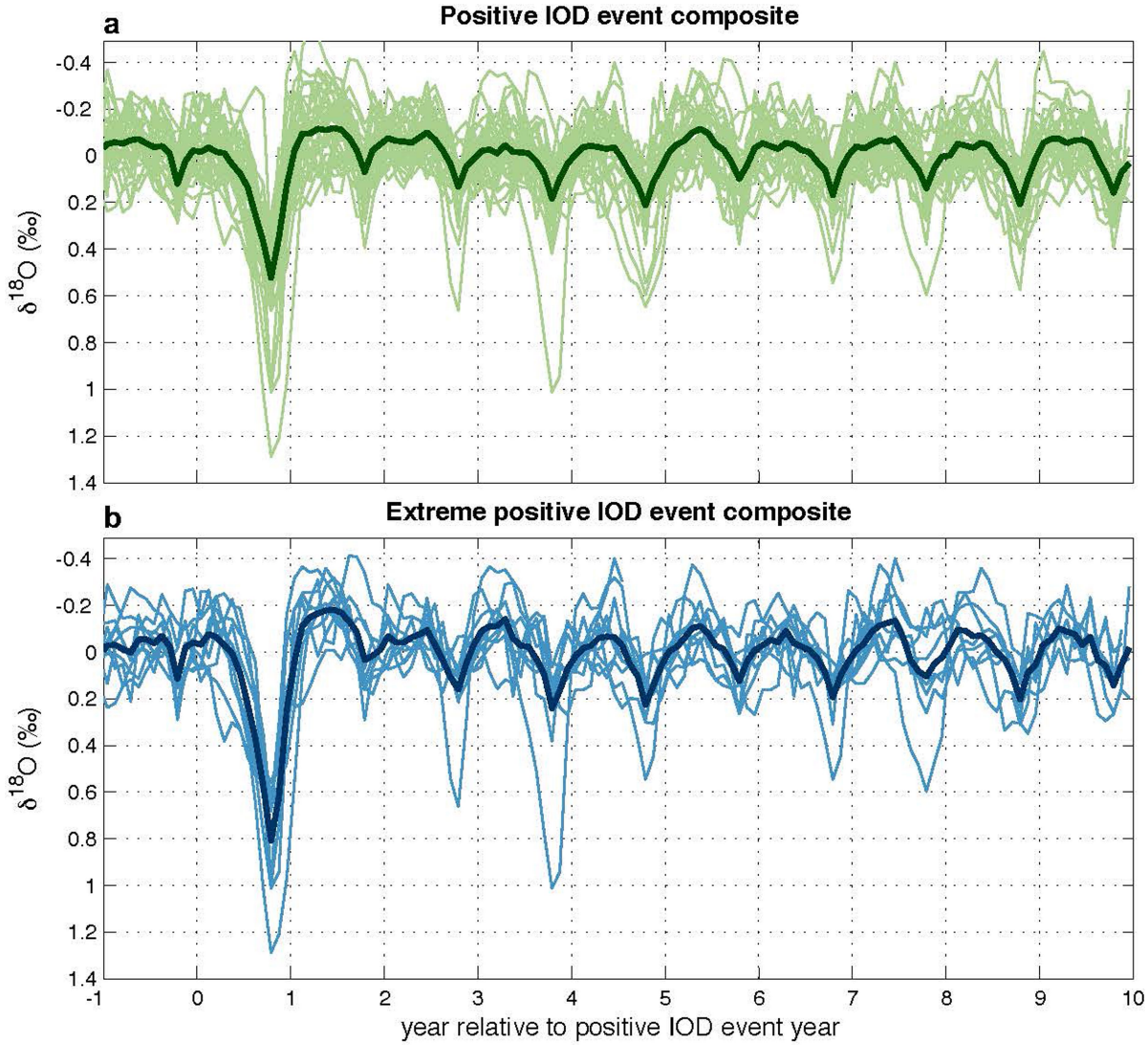


**Extended Data Fig. 5 | Composite time series for positive IOD events.** **a**, **b**, Composite records (bold curves) of coral $\delta^{18}O$ anomalies for all positive IOD events (thin green curves based on 33 events) (**a**) and all extreme positive IOD events (thin blue curves based on 10 events) (**b**) in the last millennium coral reconstruction. Composites are aligned such that positive IOD events occur within July–December of year 0.

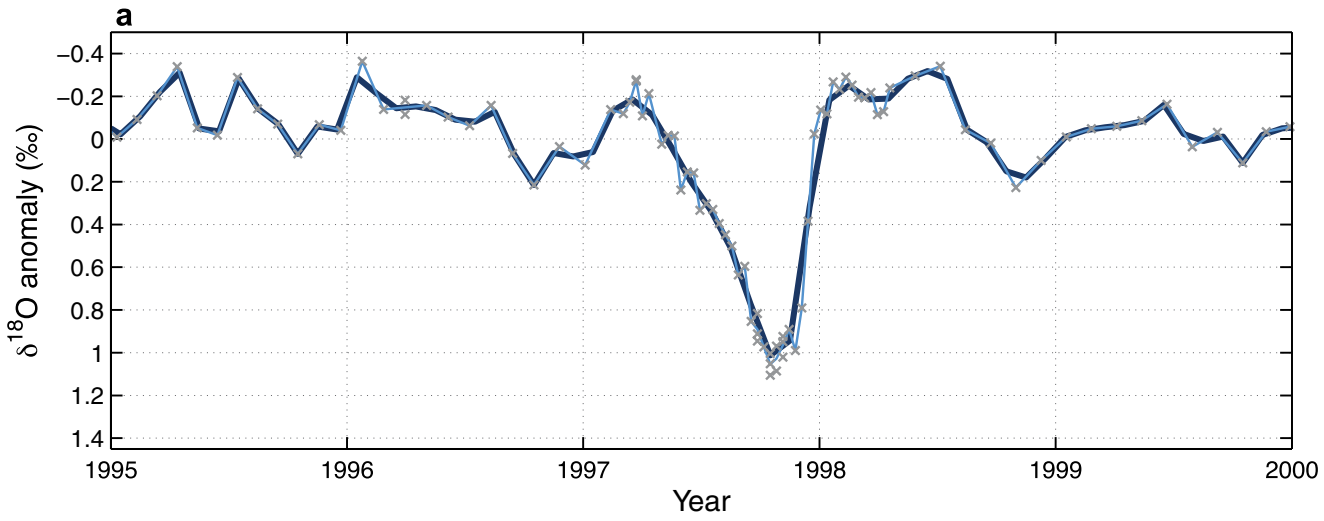


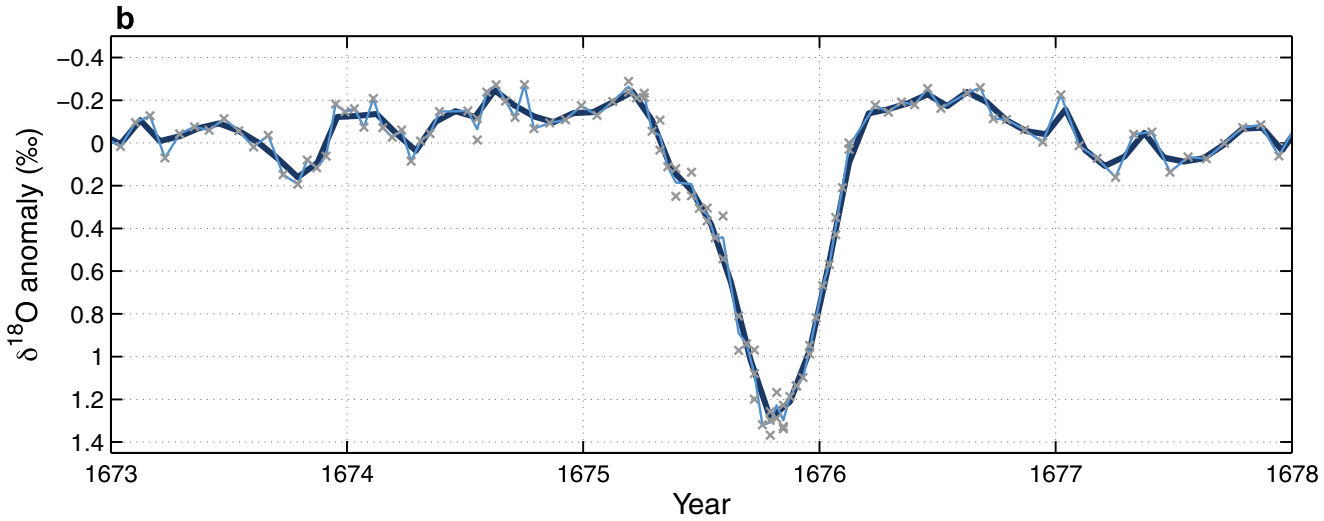


**c**

| Extreme positive IOD event year | Peak monthly $\delta^{18}O$ anomaly | Peak magnitude relative to 1997 | July-December mean $\delta^{18}O$ anomaly | July-December mean relative to 1997 |
|---|---|---|---|---|
| 1997 | 1.01 ± 0.01 ‰ | | 0.65 ‰ | |
| 1994 | 0.98 ‰ | -3% | 0.46 ‰ | -29% |
| 1961 | 1.00 ‰ | -2% | 0.44 ‰ | -33% |
| 1877 | 0.68 ‰ | -6% | 0.30 ‰ | -26% |
| 1675 | 1.29 ± 0.01 ‰ | +27% | 0.92 ‰ | +42% |
| 1660 | 0.60 ‰ | -41% | 0.44 ‰ | -32% |
| 1653 | 0.65 ‰ | -36% | 0.54 ‰ | -17% |
| 1584 | 0.66 ‰ | -35% | 0.35 ‰ | -46% |
| 1251 | 0.56 ‰ | -45% | 0.40 ‰ | -38% |

**Extended Data Fig. 6 | Extreme positive IOD events in the last millennium.** **a**, **b**, Detailed comparison of coral $\delta^{18}O$ anomalies during the 1997 (**a**) and 1675 (**b**) extreme positive IOD events, showing monthly average anomalies (thick dark blue lines), the non-interpolated $\delta^{18}O$ anomaly data (thin light blue lines) and the raw $\delta^{18}O$ anomaly measurements demonstrating replicate analyses across the extreme positive IOD events (grey crosses). **c**, Details of the extreme positive IOD event years identified in the last millennium IOD reconstruction (Fig. 2), giving the peak monthly mean $\delta^{18}O$ anomaly and the July–December mean $\delta^{18}O$ anomaly for each event, and the magnitude of these isotopic anomalies relative to the 1997 extreme positive IOD event. We note that coral $\delta^{18}O$ data for the 1877 event is based on a previously published northern Mentawai Islands sample[48], and its magnitude is assessed relative to 1997 coral $\delta^{18}O$ data from the northern Mentawai Islands. See Methods for details on chronological constraints and uncertainties on absolute fossil coral ages.

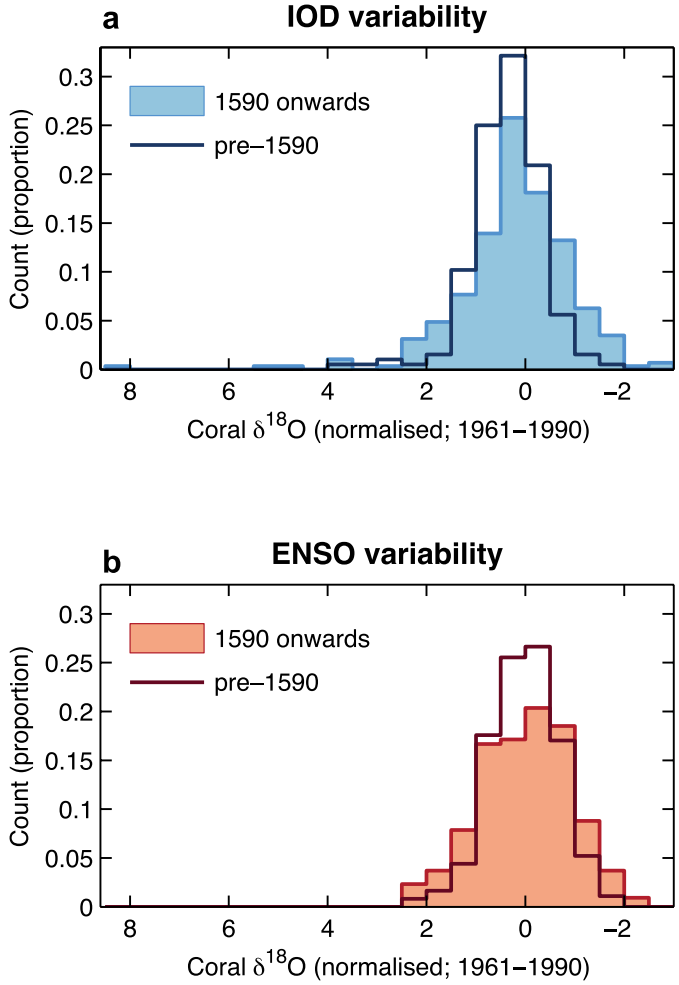


**Extended Data Fig. 7 | Mid-millennium shift in IOD and ENSO variability.** **a**, **b**, Distributions of coral $\delta^{18}O$ before 1590 and from 1590 onwards demonstrate changes in IOD (**a**) and ENSO (**b**) variability during the mid-millennium. Identification of a mid-millennium shift in IOD–ENSO variability to around 1590 (Fig. 3) is based on the time when the 30-year IOD variability in the sixteenth-century coral sequence transitioned from negative to positive amplitude anomalies (relative to 1961–1990). Distributions shown here are based on July–December average data for the IOD reconstruction, and July–June average data for the ENSO reconstruction, with $\delta^{18}O$ normalized relative to the 1961–1990 interval. For the IOD reconstruction the distributions are derived from 196 years of coral data before 1590, and 286 years of coral data from 1590 onwards. For the ENSO reconstruction the distributions are derived from 364 years of coral data before 1590, and from 216 years of data after 1590. Statistical testing (Kolmogorov–Smirnov test) indicates that the pre-1590 distributions are significantly narrower (reduced range of variability) than distributions of data from 1590 onwards for both the IOD and ENSO reconstructions ($P = 0.0004$ for IOD changes, and $P = 0.04$ for ENSO changes). Moving application of this distribution testing further confirms that minimum $P$ values are achieved if the mid-millennium shift is placed during the 1590s; specifically 1591 (1598) based on the Kolmogorov–Smirnov (Wilcoxon rank-sum) method.

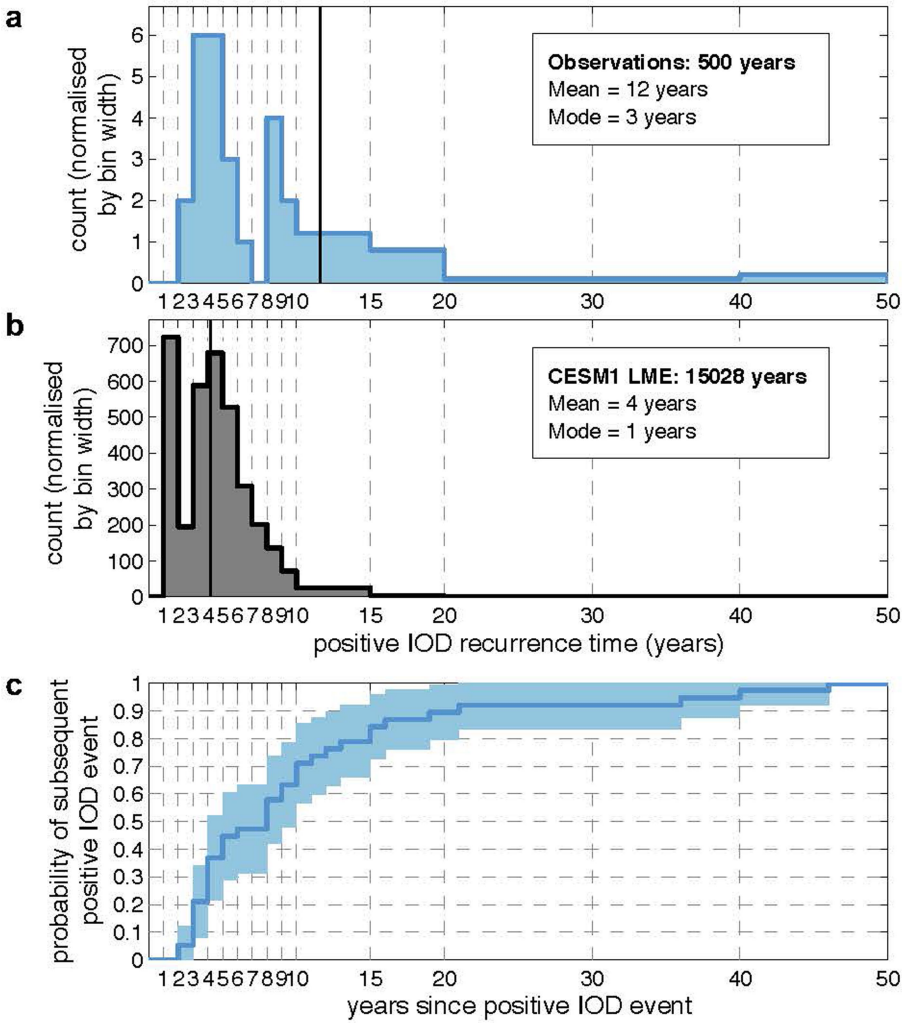


**Extended Data Fig. 8 | Recurrence times between positive IOD events.** **a**, **b**, Distributions for the recurrence times between positive IOD events in the coral reconstruction (blue) (**a**) and the CESM1-LME simulations (black) (**b**). Vertical black line denotes the mean interval between positive IOD events across the full timeseries. **c**, The cumulative probability of subsequent positive IOD events, based on years since the previous event, was assessed across the last millennium IOD reconstruction using a Kaplan–Meier estimate (blue curve) with 95% confidence bounds (shading).

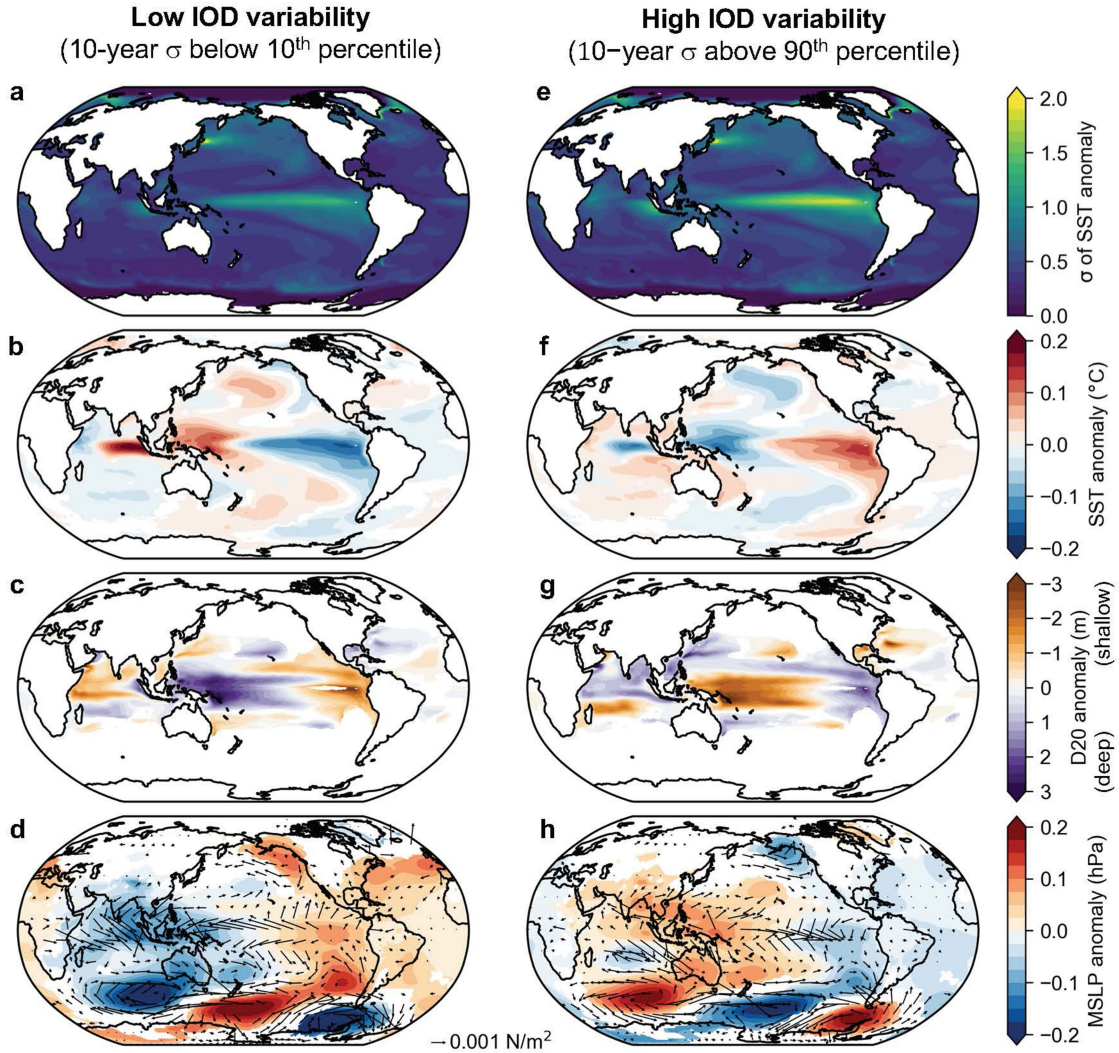


**Extended Data Fig. 9 | Coupling of IOD–ENSO variability in last millennium simulations.** Composite maps as in Fig. 4c–j, but based on 10-year standard deviation of IOD variability. **a**–**d**, Composite maps of standard deviation of July–December SST anomalies (**a**), and July–December averages of anomalies of SST (**b**), depth of the 20 °C isotherm (D20) (**c**) and mean sea level pressure (MSLP; shading) and surface wind stress (arrows) (**d**), calculated across all 10-year intervals where July–December IOD variability was below the 10th percentile in the CESM1-LME full forcing ensemble. **e**–**h**, as in **a**–**d**, but composited across all 10-year intervals where IOD variability was above the 90th percentile. Data are shown only for grid cells where distributions between intervals of low and high IOD variability are significantly ($P < 0.05$) different based on a Kolmogorov–Smirnov test. Composite maps show the same spatial pattern of climate anomalies as in Fig. 4, but with greater amplitude owing to the shorter compositing window.

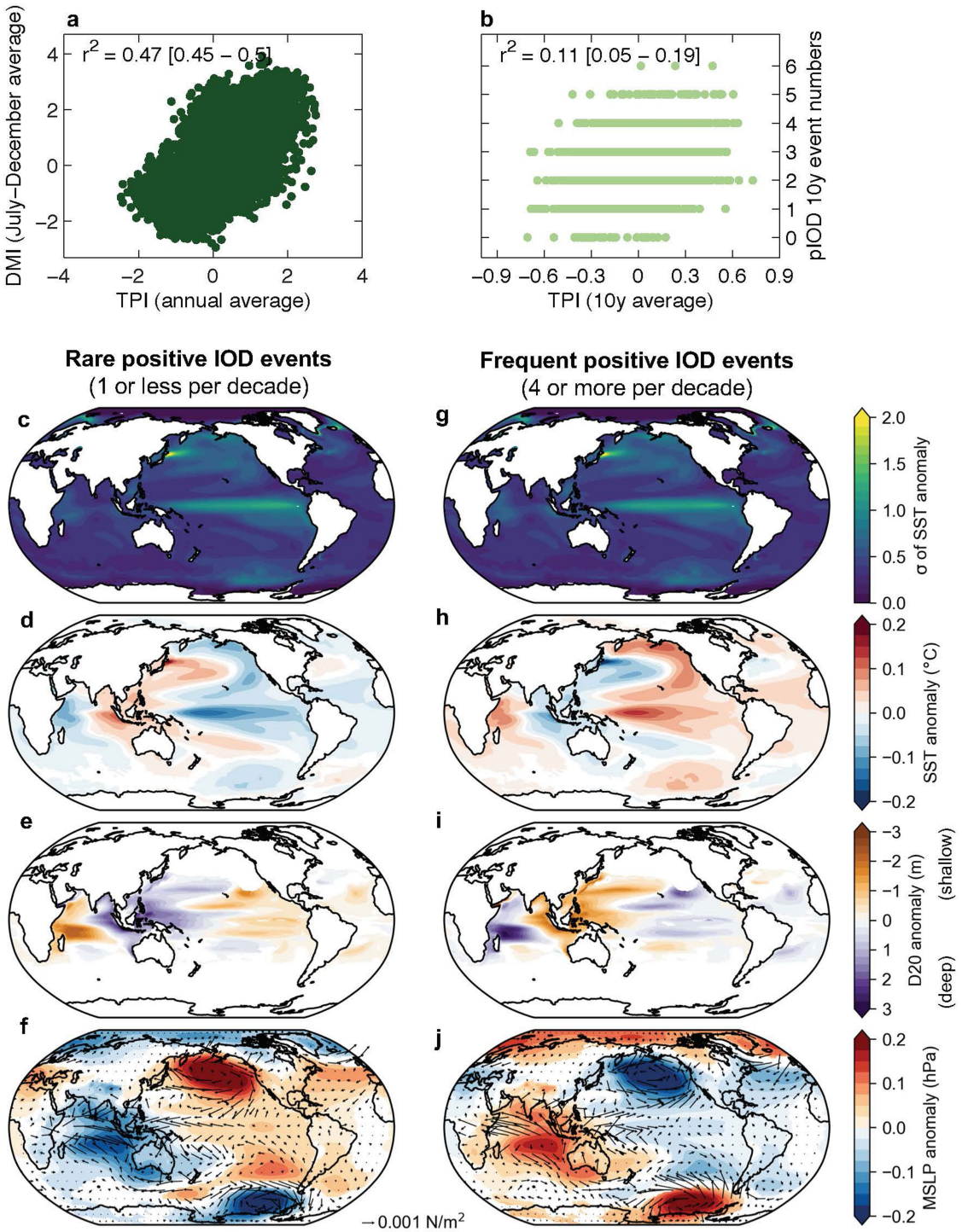


**Extended Data Fig. 10 | Decadal modulation of positive IOD event frequency in last millennium simulations. a**, **b**, Scatter plots of the modelled DMI (**a**) against the Tripole Index (TPI) of the Interdecadal Pacific Oscillation, and for 10-year positive IOD event numbers against 10-year averages of the TPI (**b**). Correlation statistics in **a** and **b** are given for aggregated data from all 13 full forcing simulations, and values in square brackets give the range of values calculated across individual simulations. **c**–**j**, Composite climate anomalies during decades of rare and frequent positive IOD events. **c**–**f**, Composite maps of standard deviation $\sigma$ of annual SST anomalies (**c**), and annual averages of anomalies of SST(**d**), depth of the 20 °C isotherm (D20) (**e**), and mean sea level pressure (shading) and surface wind stress (arrows) (**f**), calculated across all 10-year intervals containing 1 or fewer positive IOD events. **g**–**j**, As in **c**–**f**, but composited across all 10-year intervals containing 4 or more positive IOD events. Data are shown in **c**–**j** only for grid cells where distributions between intervals of rare and frequent IOD events are significantly ($P < 0.05$) different based on a Kolmogorov–Smirnov test.